PET-/SPECT-MRI Attenuation Correction using Image Registration

Studienarbeit in Computer Science
(Revised Edition)

submitted
by

Andreas Schuh

born 25th of April 1984 in Weißenburg i. Bay., Germany

Written at

Lehrstuhl für Mustererkennung (Informatik 5)
Institut für Informatik
Friedrich-Alexander-Universität Erlangen-Nürnberg.

Advisor: Dipl.-Inf. D. Hahn,
Dipl.-Inf. V. Daum,
Dipl.-Inf. J. Zeintl,
Prof. Dr.-Ing. J. Hornegger,
Prof. Dr. med. T. Kuwert (Nuclear medicine)

Started: November 15, 2007

Finished: August 15, 2008

Ich versichere, dass ich die Arbeit ohne fremde Hilfe und ohne Benutzung anderer als der angegebenen Quellen angefertigt habe und dass die Arbeit in gleicher oder ähnlicher Form noch keiner anderen Prüfungsbehörde vorgelegen hat und von dieser als Teil einer Prüfungsleistung angenommen wurde. Alle Ausführungen, die wörtlich oder sinngemäß übernommen wurden, sind als solche gekennzeichnet.

Die Richtlinien des Lehrstuhls für Studien- und Diplomarbeiten habe ich gelesen und anerkannt, insbesondere die Regelung des Nutzungsrechts.

Erlangen, den 15. August 2008

Overview

This work evaluates an MRI-guided approach to compensate PET or SPECT emission data for photon attenuation that utilizes a CT atlas and thus does not require an additional transmission scan. The introductory chapter starts with a general description of imaging in nuclear medicine, in particular molecular imaging and the desired combination of two tomographic modalities that gain functional and morphological information in one single procedure. A perspective on the future of dual-modality imaging in nuclear medicine follows, giving the motivation for the work at hand. Hereafter, the basics of the emission tomographic imaging modalities and the degrading physical phenomena which necessitate scatter and attenuation correction are presented. It is also drawn how these corrections are incorporated in the process of image reconstruction. Several developed strategies of prior art to derive the attenuation map used for both scatter and attenuation correction are delineated. The description of the evaluated approach and its mathematical model follows, where the consecutive steps are considered one by one. Afterwards, the materials and methods adopted for the evaluation and the results with the actual evaluation settings recorded are pictured. An outlook regarding the presented MRI-guided approach and a brief summary of the entire thesis completes this work, while a review of patents related to the approach can be found in the appendix.

Abstract

As the development of new imaging systems that combine PET and MRI is currently in progress, novel ideas to compensate the captured emission data for photon scatter and attenuation are being sought. A favored approach would utilize the morphological information gained from the precisely co-registered MR image to derive a patient-specific non-uniform attenuation map for accurate scatter and attenuation correction. Such a MRI-guided approach was evaluated throughout this study. A pseudo CT of the patient is obtained by inferring CT numbers from a CT atlas using automatic non-parametric registration with mutual information as distance measure and regularized by curvature. The obtained pseudo CT is then used to apply conventional methods to derive the patient-specific attenuation map from a CT image. An initial evaluation of the approach is given, where the optimal stiffness of the non-rigid transformation is determined and the mean differences of pseudo CTs generated from different atlas CTs are recorded.

Abstract

Da die Entwicklung neuer bildgebender Systeme, die PET mit MRI vereinen, derzeit voranschreitet, sind neue Ideen gefragt, um Einflüsse von Photonenstreuung und -abschwächung in den aufgenommenen Emissionsdaten auszugleichen. Ein gewünschter Ansatz würde sich der morphologischen Information des präzise co-registrierten MR Bildes bedienen und daraus eine Patienten spezifische, nicht uniforme Abschwächungskarte für exakte Streuungs- und Abschwächungskorrektur ableiten. Solch ein MRI-basierter Ansatz wurde in dieser Arbeit ausgewertet. Hierbei wird ein Pseudo CT des Patienten durch Einführen von CT Werten aus einem CT Atlas unter Verwendung automatischer, nicht-parametrischer Registrierung mit Transinformation als Distanzmaß und Regularisierung basierend auf der Krümmung des Deformationsfeldes generiert. Das erhaltene Pseudo CT wird dann durch gebräuchliche CT Bild basierte Methoden in eine Abschwächungskarte übergeführt. Eine anfängliche Auswertung des Ansatzes wurde durchgeführt, wobei die optimale Steifigkeit der nicht starren Transformation ermittelt wurde und die mittlere Abweichung der erhaltenen Pseudo CTs dargelegt ist.

Contents

Chapter 1

Imaging in Nuclear Medicine

In 1917, Johann Radon, an Austrian mathematician who later in 1925 became full professor in Erlangen, invented the Radon transform. However, Radon's original paper was virtually unknown by researchers in applied areas prior to the early 1970s. One of the investigators who independently discovered much of Radon's work was Allan M. Cormack, a physicist from Tufts University. Nevertheless, Cormack pointed out in 1973 that Radon's work was fundamental to the problem of reconstruction from projections. The first computed tomographic pictures were obtained 1970 by Godfrey N. Hounsfield. He and Allan M. Cormack were honored for their pioneer work with the Nobel Prize in physiology or medicine in 1979 [10].

To date, medical imaging modalities have attained widespread clinical acceptance as a standard of care for patients with known or suspected disease. The concept of predictive health promotes the goal of using techniques such as molecular imaging in nuclear medicine to detect and treat disease even before it has ever been expressed.

This introductory chapter explains the principles of molecular imaging. Afterwards, latest imaging devices used in nuclear medicine that combine two different modalities into a single machine are considered. These dual-modality scanners are currently the prior art to obtain functional and morphological information in one single procedure. A perspective on the future of dual-modality imaging is taken in the last section, giving the motivation for the work at hand.

1.1 Molecular Imaging

Functional imaging, as opposed to structural imaging, centers on revealing physiological activities within a certain tissue or organ. In molecular imaging, medical imaging modalities are employed that use tracers of metabolic processes to uncover their spatial distribution within the body. Tomographic modalities employed in nuclear medicine are emission computed tomography (ECT) imaging modalities, particularly Single Photon Emission Computed Tomography (SPECT) and Positron Emission Tomography (PET). In principle, their difference are the used tracers, single-photon emitters in SPECT and positron-emitters in PET.

Tracers are radioactive isotopes having similar biochemical and biological characteristics as their compounds within the body. These tracers are also called radiopharmaceuticals or radioactive labeled pharmaceuticals and have a short half-life. The short half-lives of the tracers ensure that the subject and the people handling them receive only a low radiation dose. A too long half-life furthermore would require a longer acquisition time to get reliable statistics. According to Burger and von Schulthess [6], radioactive isotopes are excellent physiologic spies to image human functional processes bound into biomolecules. In an ideal situation the corresponding non-radioactive elements occur normally in biomatter and thus a perfect spy can be synthesized. This synthetic spy is moreover not recognized as foreign by the human body. Other properties are that the images obtained by nuclear medicine contain little signal not coming from the radiopharmaceutical and that even minute quantities of radioactive spies can be detected due to the high sensitivity for detection of radioactivity.

The obtained emission data is interpreted visually and/or analyzed either semiquantitatively or quantitatively, where the extraction of quantitative information requires an appropriate mathematical model of the physiologic process to be quantified. The reason for this is that ECT measures counts only but cannot deduce in vivo to which molecular species the radioisotope is bound. PET imaging, in particular, which provides quantitative data relatively easily and at high enough temporal resolution, has seen extensive and sophisticated quantification. Input sampling of arterial or arterialized venous blood is standard even in some clinical PET studies and curve fitting using compartment modeling to derive data on perfusion, blood volume, oxygen extraction, and metabolite and receptor-ligand kinetics is widely used [6].

Besides the functional information, anatomically appropriate information is frequently obtained in bone, lung, kidney, thyroid and heart studies, while in brain studies and studies for tumor detection the anatomic information may be insufficient [6]. Fusion of functional and anatomical information obtained by structural imaging modalities such as CT and MRI is required.

1.2 Dual-modality Imaging

Different imaging modalities visualize different aspects of disease in a non-invasive way. Both CT and MRI are used primarily for imaging anatomical changes, whereas molecular imaging techniques of PET and SPECT, as introduced in the last section, capture functional or metabolic changes. Each of these two types of change delivers important information, however, only the combination of both, anatomical as well as functional information, may clarify the nature of an abnormality and help diagnose or stage the underlying disease.

Townsend and Cherry [55] described the prior art dual-modality technologies in 2001. At the time it was a novel approach to combine PET or SPECT with CT, whereas to date it is almost ordinary to have a SPECT-CT or PET-CT scanner in a clinical environment. Many of the advantages of dual-modality imaging systems besides software approaches for image fusion have been mentioned by Townsend and Cherry. One of the most obvious benefits of a combined scanner is the more accurate superposition of functional and anatomical data even in regions where fusion software hardly reveals satisfactory results. This enables a reliable localization of radiopharmaceutical uptake or guides surgery in areas where vital structures neighbor disease or in anatomically complex regions. Furthermore, the ability to acquire functional and morphological images in a single procedure increases patient throughput, which is a relevant issue in a busy clinical environment. Another opportunity offered by dual-modality scanners that combine functional and anatomical imaging modalities is the use of the morphological information for sake of precise attenuation correction (AC) of the emission data. For hybrid systems combining ECT and CT CT-based correction of the gained emission data is a method of choice.

Although the combination of ECT and CT has already attained widespread use and unless its advantages mentioned before, it has many limitations. Its major drawback is that the imaging is performed sequentially rather than simultaneously. This introduces potential misregistration due to improper patient positioning, respiratory motion and other voluntary patient movement. Lately, Goetze et al. [17] quantitatively assessed the effect of misregistration in myocardial perfusion SPECT-CT. The authors determined that misregistration of SPECT and CT occurs frequently in myocardial perfusion SPECT-CT and that it contributes significantly to changes in radiotracer distribution in the anterior, septal and inferior segments. The basic statement of these results can be carried over to general SPECT-CT and PET-CT as well, where misregistration causes artifacts in the attenuation corrected images. Moreover, CT is good at looking at the bones, whereas it governs less soft-tissue contrast without the use of contrast agents. A further important drawback of these hybrid systems is the additional radiation dose.

1.3 The Future in Dual-modality Imaging

MRI generates high resolution anatomical images offering better soft-tissue contrast and a large variety of tissue contrasts compared to CT. Additionally, MRI does not use any ionizing radiation and therefore can be used without restrictions in serial studies for pediatric cases and in many other situations where radiation exposure is a concern [67]. While the combination of PET and CT has already been realized in clinical scanners, the combination of PET and MRI is more challenging since conventional PET detectors incorporate photomultiplier tubes (PMTs) which are extremely sensitive to magnetic fields. Moreover, it is difficult to develop PET detector modules that do not cause any serious distortions or artifacts in the MR images. This can only be achieved if the use of any conducting or ferromagnetic materials is avoided to maintain the homogeneity of the main magnetic field and to minimize electromagnetic interference (EMI) between PET and MRI signals [51].

The first prototype PET detectors which are compatible with MRI systems, as the early single-slice prototype PET system developed by Shao et al. [51] and the more recently by Mackewn et al. [34] developed PET scanner for imaging small animals, coupled lutetium oxyorthosilicate (LSO) scintillator elements placed inside the magnet to PMTs and electronics placed outside the fringe of the magnetic field by 3 to 5 m long optical fibers. According to the remarks of Catana et al. [8], major limitations of this approach are the significant loss of scintillation light via the optical fibers, degrading crystal identification, energy resolution and timing resolution and that a large number of crystals is necessary to achieve both high spatial resolution and sensitivity. Because of limited space inside conventional MR magnets, it is not practical to fiber-optically couple large numbers of crystals to external electronics. Hence, a second major approach emerged where the PMTs are replaced by avalanche photodiodes (APDs) which are coupled directly to the back of the scintillators. Fortunately, APDs are relatively immune to magnetic fields and have been demonstrated to work inside MR scanners at fields as high as 9.4 T. This approach solves the many limitations of fiber-optically coupled systems but also has the largest potential for EMI between the radio frequency and gradient coils and the PET electronics. Therefore, first attempts using APDs instead of PMTs aimed at a combination of both major approaches by coupling the APDs via short lenghts of optical fibers to arrays of LSO crystals. Initial results obtained by Catana et al. [8] with such a multi-slice PET-MR scanner showed no visible artifacts using standard pulse sequences. Moreover, Judenhofer et al. [23] just recently developed a multi-slice three-dimensional animal PET scanner where the APDs are coupled directly to the back of the scintillators and therefore it could be built completely into a 7 T MRI. Already previously, Schlemmer et al. [50] presented the first human brain images with a similar

multi-slice PET-MRI system. The authors reported that the performance of neither the PET nor the MR scanner was degraded by synchronous data acquisition and that the PET and MRI data revealed image qualities comparable to stand-alone systems without any significant distortions or artifacts. Particularly, the integrated PET detector was invisible for the MRI system maintaining a good signal-to-noise ratio (SNR) and spectral resolution of MR spectroscopy (MRS).

Besides the difficulties to combine PET and MRI, it provides several more potential advantages compared to PET-CT as only the high soft-tissue contrast and elimination of additional ionizing radiation. Simultaneous imaging of function and morphology becomes possible, thus, greatly reducing the amount of misregistration if not even eliminating it. The accurate registration furthermore permits precise anatomically based region of interest definition and may allow partial volume correction for PET data. In addition, this technology could be used to directly compare functional MRI (fMRI) studies with PET blood flow studies and to temporally correlate MRS and PET information in the study of complex metabolic processes and is capable of assessing flow, diffusion, perfusion and cardiac motion in one single examination [51, 67]. Zaidi stated in the point/counterpoint discussion if PET-MRI will replace PET-CT as the molecular multi-modality imaging platform of choice in [67], that PET-MRI will likely succeed in unifying the four promising molecular imaging techniques PET, MRI, fMRI and MRS, which be in sharp contrast to the limited information provided by dual-modality PET-CT.

However, in comparison to CT, MRI produces anatomical images from which it is more difficult to derive attenuation maps for correction of the emission data. In an only recently published article [65] again Zaidi stated if MRI-guided attenuation correction is a viable option for dual-modality PET-MR imaging. In this article he summarized the few studies that have addressed this issue so far and concluded that the results are still unconvincing and more research is needed. Nevertheless, the feasibility of some approaches has yet been demonstrated and the motivation for the work at hand as well was to evaluate the feasibility of another MRI-guided attenuation correction strategy for PET-MR scanners.

Chapter 2

Emission Tomography

In transmission tomography a gamma source is placed outside the human body and the attenuation of photons traveling through the body is pictured. Contrary, in emission tomography the subject has been injected with, has ingested or has inhaled a radioactive tracer that radiates photons. Detectors then collect the endogeneous photons from outside the body. The measured radiation is directly related to a physiological metabolism of the examined subject. The kind of physiological function that is imaged is determined by the administered radioactive tracer. An isotope compound of glucose, for instance, can be used to identify areas of cancerous involvement and to distinguish malignant from benign lesions. It therefore plays an important role in the diagnosis and management of patients with cancer.

This chapter gives at first a description of the commonly used ECT modalities in nuclear medicine. Afterwards, the effect of photon attenuation in emission tomography is treated in detail. Which algorithms are used to reconstruct the emission images is considered towards the end of this chapter. The attention there is turned on the compensation for photon attenuation.

2.1 Single Photon Emission Computed Tomography

Single Photon Emission Computed Tomography is the direct progression of planar scintigraphy. While planar scintigraphy is comparable with radiography, SPECT can be compared with CT. A gamma camera invented by Hal O. Anger [2] in 1957 and therefore also known as Anger camera is used to capture the photons emitted by the tracer.

The gamma camera consists of a mechanical collimator, a scintillation crystal, an array of PMTs and a processing unit including a discrimination unit to separate scattered from unscattered photons. The schematic representation of the gamma camera is shown in Figure 2.1. Photons emitted by the radiopharmaceutical are detected as described in the following. The collimator ensures that each photon impinging on the detector has a well-defined direction such that the corresponding projection line can be determined. This is necessary for tomographic reconstruction of the emission image. A photon that enters the scintillator interacts with the crystal atoms until it has lost all its energy, whereby the atoms are raised to an excited state. The excited atoms return to the ground state by emitting visible-light photons that can traverse the scintillation crystal unresisted. These light photons reach the light-sensitive surface of the neighboring PMTs causing a photoelectric effect and so releasing electrons. These are multiplied by a cascade of stages in the PMTs and the generated currents are further amplified. The amplified currents are proportional to the number of light photons that hit the corresponding PMT. Hence, the overall current is proportional to the total number of scintillation photons and therefore proportional to the energy of the impinged photon. Moreover, the PMTs get an amount of light that depends on their relative position to the scintillation event, which enables the decoding of the location where the photon has impinged on the crystal. The discrimination unit takes the overall current proportional to the photon energy and compares it to the expected current corresponding to the energy of the photons emitted by the radionuclide used. Scattered photons have lost part of their energy and thus can be discarded by the discrimination unit. However, many of the processes involved in detection underly statistical variations and the estimated energy therefore also shows a Gaussian distribution around the true value, known as the photopeak. The broader the peak, the worse is the energy resolution of the gamma camera. Scattered photons that are still under the photopeak cannot be distinguished from primary, unscattered photons. The range of energy that is accepted by the discrimination unit is called the photopeak window. Each accepted event in the photopeak window increments the counter of the corresponding pixel in the image matrix [6, 13].

nuclide	half-life	E_γ (keV)
^{99m}Tc	6 h	140
^{123}I	13 h	159
^{201}Tl	3.1 d	80 + 167
^{67}Ga	3.2 d	92 + 185 + 296
^{111}In	2.8 d	173 + 247

Table 2.1: Properties of commonly used radionuclides in SPECT

tracer	organ	diagnostic question
^{99}Tc-Phosphate	bone	tumor
^{99}Tc-Phosphate, ^{201}Th-Chloride	heart	septal defects, stroke volume
^{99}Tc-Pertechnetate	thyroid	tumor, hyperfunction
^{99}Tc-Macroalbumine	lungs	ventilation

Table 2.2: Commonly used tracers in SPECT and their fields of application

Instead of acquiring just a single planar projection of the spatial distribution of radioactivity, as it is the case in planar scintigraphy, multiple projections are drawn from different angles about the patient, where several slices are acquired simultaneously. The projections obtained are then reconstructed in the same manner as it is done in CT. There are basically two solutions to obtain the required projections. So called multi-detector systems consist of a closed ring or polygon of detectors into which the body section of interest is placed. To date, these systems are dedicated to brain studies and not in widespread use. The favored solution is a gantry with one or more movable heads as illustrated in Figure 2.2 [6]. An important not illustrated configuration is the triple-head SPECT system, where one of the gamma cameras is used to acquire transmission data from an opposite radionuclide source additionally to the emission data if radionuclide transmission imaging is applied to obtain the attenuation map. A nice property of a dual-head SPECT system is that it can easily be upgraded to a relatively cheap PET system by just attaching a coincidence detection circuit, resulting in a combined SPECT-PET system [13].

For the SPECT radionuclides, photon energy is ideally in the range of 100 to 200 keV. Below 100 keV tissue absorption and scatter become significant, whereas above 200 keV there is low detection efficiency. Typical radionuclides used in SPECT and their properties are listed in Table 2.1 [15], whereas Table 2.2 lists common tracers and their fields of application [13].

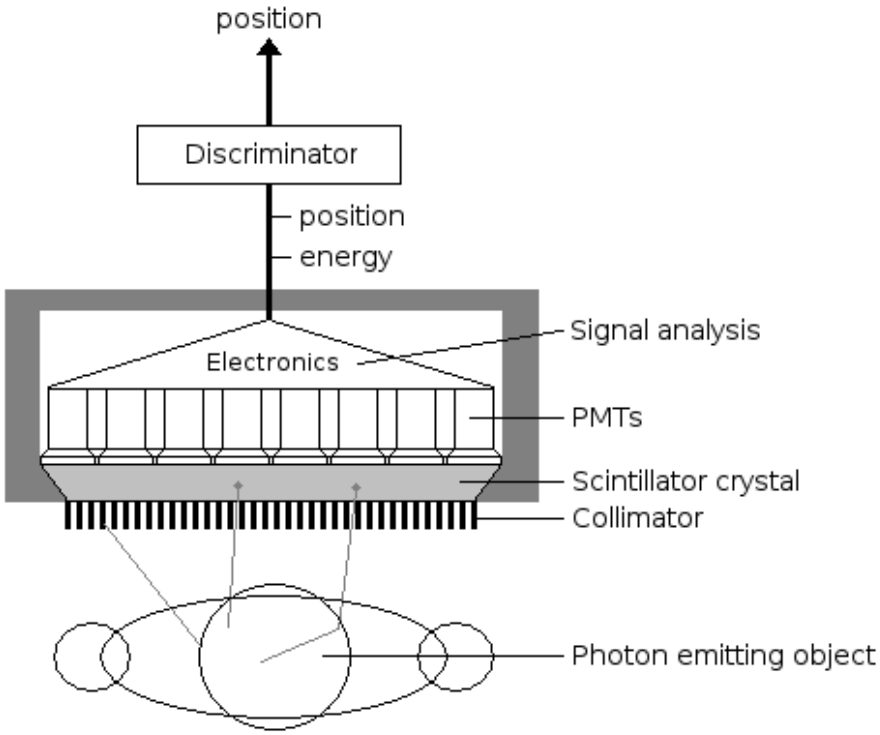

Figure 2.1: Schematic representation of the gamma camera

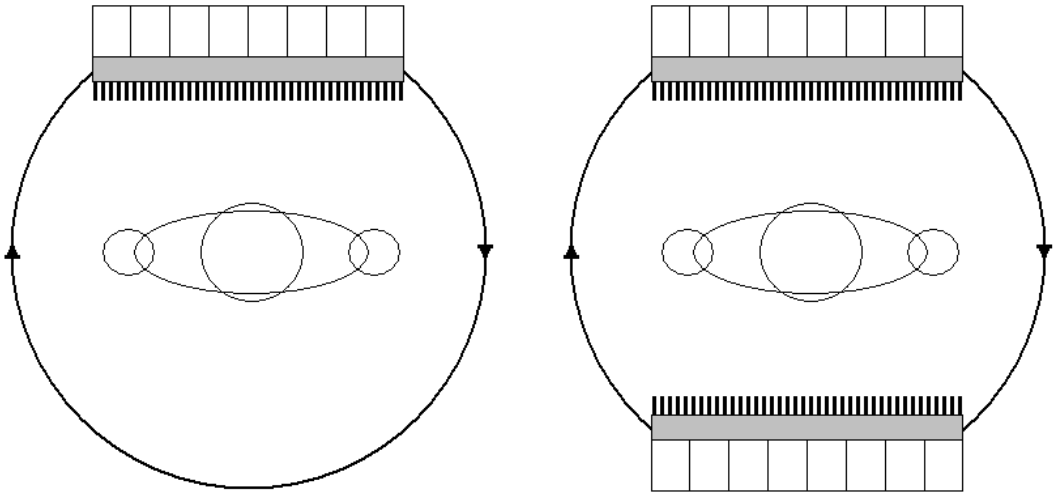

(a) single-head (b) dual-head

Figure 2.2: SPECT systems

2.2 Positron Emission Tomography

Tracers in Positron Emission Tomography are positron emitters. Typical radionuclides used and their properties are listed in Table 2.3 [40, 49]. On decay a proton turns into a positron, a neutron and a neutrino [40]:

$$\mathrm{p} \rightarrow \mathrm{e}^{+} + \mathrm{n} + \nu \; .$$

The range of the emitted positrons lies within few millimeters. Within this range the positrons are slowed down due to interactions with neighboring atoms and finally each annihilates with an electron. The result of the annihilation are two photons traveling in opposite direction [40]:

$$\mathrm{e}^{+} + \mathrm{e}^{-} \rightarrow 2\gamma \; .$$

Due to the law of the conservation of energy and momentum, the energy of each photon is 511 keV. The annihilation photons are detected by a ring of detectors enclosing the patient body in a 360° circle. Mainly due to statistical components in the detection and processing time, both single events may have a time delay. Thus, single events that are detected within a coincidence time window of usually 10 to 20 ns are considered as simultaneous and belonging to a single positron annihilation. According to Newiger [40] a typical time window for coincidence detection is about 12 ns long. Each recorded coincidence increases the count of the projection ray corresponding to the so called line of response (LOR) connecting the opposing detectors which registered the two single events. Not only true coincidences but also random or scattered coincidences are erroneously recorded. Thus, the acquired projection data has to be corrected for these effects. The positron decay and annihilation as well as the detection of the coincidence is illustrated in Figure 2.3 [40, 6, 13].

Besides some alternative PET system designs as described in [6], multi-ring PET scanners are commonly used. These scanners have several adjacent detector rings that are housed in a gantry and can operate either in 2D or 3D mode. Each of these rings consists of so called block detectors, each in turn consisting of an array of, for instance, four by eight crystals with four PMTs. The detector rings acquire projections in many directions simultaneously. A system operating in 2D mode, in principle, images transaxial planes of the investigated part of the body independently. Therefore, the rings are separated by tungsten septa. An important aspect of PET scanners is that no further mechanical collimation takes place, since the detection of only coincidence events performs even an electronic collimation. A property of electronic collimation and simultaneous acquisition of projections is the acquisition of sufficient statistics with less activity.

nuclide	half-life (min)	max. $E_{\beta+}$ (MeV)	average $E_{\beta+}$ (MeV)	max. range (mm)	average range (mm)
^{11}C	20.4	0.96	0.385	5.0	0.3
^{13}N	9.9	1.19	0.491	5.4	0.4
^{15}O	2.9	1.72	0.735	8.2	1.5
^{18}F	110.0	0.64	0.242	2.4	0.2

Table 2.3: Properties of commonly used radionuclides in PET

tracer	measurement of	fields of application
^{11}C-Acetate	fatty acid metabolism	cardiology
^{11}C-Methionine	amino acid metabolism	oncology
^{13}N-NH_3	perfusion	cardiology
$H_2{}^{15}O$	perfusion	cardiology, neurology
^{18}F-FDG	glucose metabolism	cardiology, neurology, oncology

Table 2.4: Commonly used tracers in PET and their fields of application

In 3D mode the septa are removed to exploit as much information as possible. However, also the detection of scattered coincidences increases significantly. Figure 2.4 illustrates the difference in LORs of a multi-ring PET scanner operating in 2D or 3D mode [6].

According to [6] there are two fundamental processes that limit the resolution obtainable with PET: the range of the positrons between emission and annihilation and the deviation from exact collinearity of the two emitted annihilation photons. The average range of commonly used positrons can be taken from Table 2.3 and is dependent on the kinetic energy of the positrons. Since the positrons are still moving when they meet an electron, the angle between the two emitted photons is not exactly 180° but show an almost Gaussian distribution with a full width at half maximum of about 0.5°. A deviation from 180° causes the annihilation to be located on a wrong line. Hence, the fundamental resolution limit is about 3 mm, whereas current PET scanners achieve a resolution of 4 to 6 mm at the center of the field of view (FOV). Moreover, the resolution increases with less recorded events since the high frequencies have to be cut off during reconstruction [13].

Typical clinical applications of PET show up in cardiology, neurology and especially oncology, where, for example, tumor growth and metabolism can be pictured quantitatively to guide patient treatment and to monitor the success of a therapy. Table 2.4 lists tracers commonly used in PET and their fields of application [40].

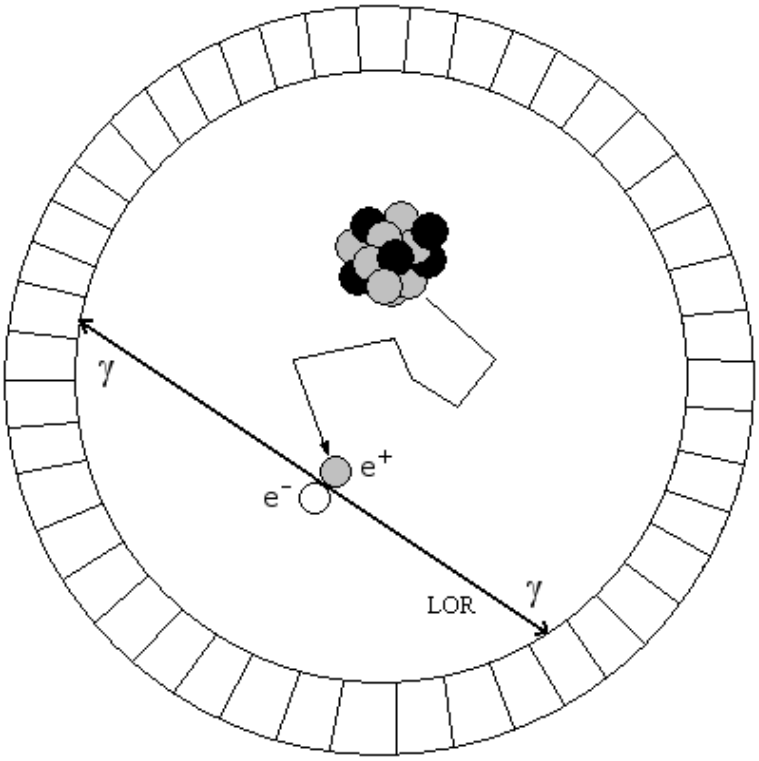

Figure 2.3: Illustration of positron decay and annihilation

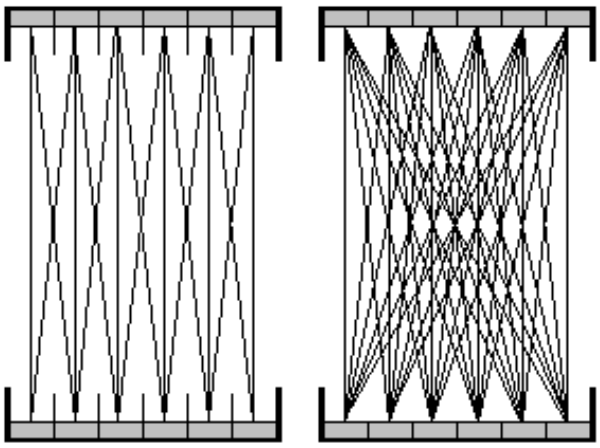

(a) 2D mode with septa in (b) 3D mode with septa out

Figure 2.4: LORs of a multi-ring PET scanner in 2D and 3D modes

2.3 Photon Attenuation

A radiopharmaceutical used for radionuclide imaging gets distributed in the body, emitting photons at one or more energies. Starting from the point of its generation, a photon travels along a straight line until it interacts with matter. In the desired case this happens within the detector outside the body and results in an event that is recorded. However, if the photon interacts with body matter on its way to the detector, it is absorbed or deflected from its original direction [6]. Both absorption and scattering are the components of the general process of photon attenuation.

2.3.1 Interactions of Radiation with Matter

At the photon energies below 1000 keV encountered in nuclear medicine the major interactions in body tissues are photoelectric absorption and Compton scattering. Photoelectric absorption dominates over scattering for photons of low energy and dense absorbers. The total attenuation is dominated by the photoelectric effect below photon energies of 30 keV and 50 keV for soft tissue and bone and is dominated by Compton scattering for photon energies between 200 to 1000 keV [28].

Photoelectric Effect In the photoelectric effect, illustrated in Figure 2.5, the incident photon transfers all its energy to an orbital electron of the absorber atom. This photoelectron is ejected from the atom with a kinetic energy E_{kin} equal to the photon energy E_γ reduced by the electrons' binding energy E_{b}:

$$E_{\mathrm{kin}} = E_\gamma - E_{\mathrm{b}} \; . \tag{2.1}$$

The photoelectron looses its energy by ionization and excitation in the absorber, which enables the detection of the photon in the detector as described in section 2.1. The photoelectric effect occurs primarily for low-energy photons and decreases sharply with increasing photon energy and very rapidly with decreasing atomic number Z of the absorber atom. Roughly, it is proportional to Z^5/E_γ^3. Moreover, it occurs primarily with the K-shell electrons, with about 20% contribution from the L-shell electrons and even less from higher shells. There are sharp increases in photoelectric effects at energies exactly equal to binding energies of the shell electrons [49].

Compton Scattering In Compton scattering, illustrated in Figure 2.6, the photon strikes a loosely bound electron of an absorber atom of body tissue and transfers a part of its energy E_γ to it. The Compton electron is ejected from the absorber atom and may cause ionization or excitation as in the photoelectric effect. The photon itself is deflected from its original direction at the angle θ, continuing with less energy $E_{\gamma'}$. It may undergo subsequent interactions in the absorber or may escape without further interaction. Using the law of the conservation of momentum and energy, the scattered photon energy is given by [49]:

$$E_{\gamma'} = \frac{E_\gamma}{1 + (E_\gamma / m_e c^2)(1 - \cos\theta)} \ , \tag{2.2}$$

where m_e is the rest mass of an electron and c is the light speed. Thus, the product $m_e c^2$ is equal to 511 keV, the rest energy of an electron. Moreover, the kinetic energy E_{kin} of the Compton electron is given by:

$$E_{\text{kin}} = E_\gamma - E_{\gamma'} - E_{\text{b}} \ , \tag{2.3}$$

where E_{b} is the binding energy of the Compton electron. Compton scattering is directly proportional to the atomic number Z and has a slight non-linear inverse dependence on photon energy between 10 and 1000 keV. At low photon energies, forward and backward scattering is equally likely, but at higher energies, scattering in forward direction dominates more [49, 28, 6].

2.3.2 Linear and Mass Attenuation Coefficient

The intensity of transmitted photons through an absorber can be expressed mathematically by the exponential equation [62]:

$$I = I_0 \ \exp\left[- \int_L \mu(\boldsymbol{x}) dl \right] \ , \tag{2.4}$$

where I_0 is the intensity of incident photons and dl is a differential of the thickness of matter encountered as the beam of photons passes through the absorber along path L. The function μ is the spatial distribution of the linear attenuation coefficients. The attenuation coefficient μ at a specific spatial location $\boldsymbol{x}$ represents the probability that a photon will undergo an interaction while passing through a unit thickness of matter. It is therefore a measure of the fraction of primary photons that interact with the absorber and is expressed in cm^{-1} [6, 62].

The linear attenuation coefficient μ is dependent on the photon energy and proportional to the density of the absorber. To compare the attenuation of different materials, the linear attenuation coefficient of a material is divided by its density ρ to form the mass attenuation coefficient μ_m in cm^2/g, which then depends only on the photon energy [6]:

$$\mu_m := \frac{\mu}{\rho} \, . \tag{2.5}$$

From [62] it can be concluded that bone suffers more attenuation than lung tissue and that the photons appearing in SPECT are more attenuated than the annihilation photons occurring in PET.

In the case considered above, the intensity of transmitted photons excludes scattered photons that are erroneously recorded as events. This is called the good geometry condition and the linear attenuation coefficients in this case are referred to as narrow-beam attenuation coefficients. Otherwise, if scattered photons are included, they are referred to as broad-beam attenuation coefficients. The build-up factor originating from the broad-beam condition is defined as the ratio of the total transmitted photons divided by the ideal narrow-beam measurement corresponding to unscattered photons in the transmitted beam. Thus, the build-up factor on the good geometry condition is equal to one, but greater than one on the broad-beam condition [70].

The exponential equation for the broad-beam condition is given by:

$$I = I_0 B \, \exp\left[- \int_L \mu(\boldsymbol{x}) dl \right] , \tag{2.6}$$

where B is the build-up factor caused by scattered photons. Zaidi et al. [70] summarized the fundamental relationship of scatter to attenuation. According to them, a photoelectric absorption contributes only to attenuation, but Compton scatter increases attenuation and also sets up a potential scatter corruption. Attenuation and scatter have opposite effects on activity quantification in the sense that photon attenuation decreases counts, thus allowing too few photons to be detected, resulting in underestimation of activity. In contrast, scatter corruption increases counts, thus allowing too many photons to be detected, resulting in overestimation of activity. Both uncorrected attenuation and uncorrected scatter corruption cause significant loss of contrast between neighboring structures and bias in activity quantification.

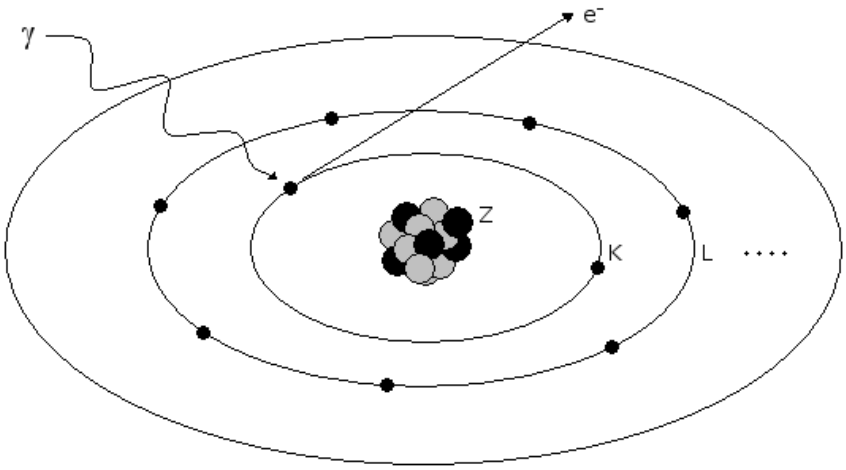

Figure 2.5: Photoelectric effect

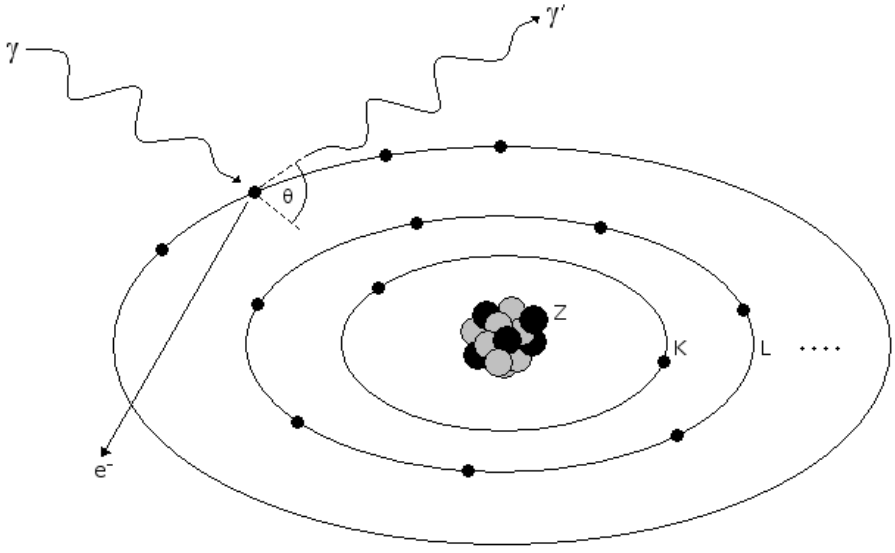

Figure 2.6: Compton scattering

2.4 Reconstruction

Once the emission data has been collected, a reconstruction algorithm is applied to get the tomographic images of the spatial distribution of radioactivity. The mathematical foundation of reconstruction in computerized tomographic imaging is based on the Radon transform [10]:

$$p(\theta, t) = \int_{L(\theta,t)} f(x, y) dl \ , \tag{2.7}$$

where a two-dimensional parallel geometry is considered. The parameter θ represents the projection angle, t the transverse position and f the radionuclide source distribution. The projection line L is given by:

$$x \ \cos \ \theta + y \ \sin \ \theta = t \ . \tag{2.8}$$

Fourier methods on the basis of the Fourier Slice theorem, namely filtered backprojection (FBP) [24, Chapter 3], and algebraic reconstruction algorithms [24, Chapter 7] have been used for decades to solve the reconstruction from projections problem.

The above equation (2.7) holds in emission tomography only if the attenuating properties of the object can be omitted. This is hardly true in the case of human subjects. Not minding the attenuation of photons leads to serious artifacts in the reconstructed images. These artifacts make it difficult or even impossible to read the images and to make a reliable diagnose. Particularly, if quantitative analysis of the physiologic processes is desired, compensation for photon attenuation is mandatory. Bai et al. [3] investigated the effects of attenuation on tumor detection in whole-body PET imaging and strongly recommended the application of attenuation correction strategies to avoid missing regions of elevated tracer uptake. Moreover, as another example to note its importance, professional societies recommended attenuation correction for myocardial perfusion SPECT in a joint position statement [19]. Figure 2.7 illustrates the reconstruction artifacts if the emission projections are reconstructed without attenuation correction.

Therefore, the spatial distribution of linear attenuation coefficients has to be incorporated into equation (2.7). The amount of attenuated photons in SPECT depends on the tissue pathlength that the photon encounters as it travels between the point of emission and the point of detection, whereas in PET the annihilation photons traverse a total tissue thickness that is equal to the body thickness intersected by the LOR. Accordingly, the path L in equations (2.4) and (2.6), respectively, is the path from the point of emission to the point of detection in SPECT but the whole LOR in PET. Attention has therefore to be paid to the difference in paths resulting in slightly different formulas for SPECT and PET [62].

The general equation describing measured projections in terms of the radionuclide source distribution inside an attenuating medium is given in the case of SPECT by:

$$p_{\mathrm{SPECT}}(\theta,t) = \int_{L(\theta,t)} f(x,y)\ \exp\left[-\int_0^{d(x,y)} \mu(x',y')dl'\right] dl\ , \tag{2.9}$$

where d is the distance from the emission point in the object to the detector along the projection line and μ is the spatial distribution of narrow-beam attenuation coefficients. Whereas the attenuated Radon transform in PET is given by:

$$p_{\mathrm{PET}}(\theta,t) = \int_{L(\theta,t)} f(x,y)dl \times \exp\left[-\int_{L(\theta,t)} \mu(x,y)dl\right]\ . \tag{2.10}$$

Nevertheless, as the amount of attenuation is independent of the point of emission along the LOR, the captured sinograms in PET can exactly be corrected for attenuation by simple pre-multiplication with attenuation correction factors (ACFs) obtained by transmission imaging as described in section 3.2.1 or calculated from a patient-specific attenuation map, provided such a μ-map is available. The ACFs are defined as the exponential of the line integrals of linear attenuation coefficients along each LOR [70]:

$$ACF(\theta,t) := \exp\left[\int_{L(\theta,t)} \mu(x,y)dl\right]\ . \tag{2.11}$$

The corrected projections are obtained as noted above by simple pre-multiplication [70]:

$$p_{\mathrm{PET,AC}}(\theta,t) = ACF(\theta,t) \times p_{\mathrm{PET}}(\theta,t) = \int_{L(\theta,t)} f(x,y)dl\ . \tag{2.12}$$

However, attenuation correction is more complicated and can only be an approximation in SPECT, because the attenuation factors cannot be separated from the unattenuated Radon transform. Apart from that it should be noted that the magnitude of the ACFs required in PET is far greater than in SPECT [62]. In addition, correction for events generated by scattered photons and random coincidences in PET have been neglected so far. Not applying any scatter correction in conjunction with attenuation correction results in overestimation while compensating for attenuation alone. Thus, the build-up factor caused by scatter has to be estimated and compensated for. This is done in PET prior to the attenuation correction as described above. In [68], Zaidi and Montandon only recently gave an exhaustive overview of scatter correction techniques commonly applied in PET.

(a) AC PET image (b) Non-AC PET image

Figure 2.7: Reconstructed PET image with and without compensation for photon attenuation

King et al. [26] reported increased artifacts when the spatial resolution in the attenuation map was either significantly better or worse than the resolution of the emission data being corrected. Thus, if the attenuation map has higher spatial resolution, additional smoothing can be used to reduce noise and to match the resolution to that of the emission image.

Although FBP has been the most common technique for image reconstruction in CT and also ECT for many years, it can in general only be an approximation to the inverse attenuated Radon transform with non-uniform attenuation [62]. This and the advantages of iterative reconstruction algorithms mentioned below, which also enable compensation for scatter and attenuation in SPECT, led to increasingly use of iterative algorithms, particularly the maximum likelihood expectation maximization (ML-EM) algorithms first introduced by Rockmore and Macovski [48]. A practical implementation of the EM method was introduced in PET by Shepp and Vardi [52]. Kontaxakis and Strauss [30] published a conspicuous survey of applied maximum likelihood algorithms. The authors list many of the important modifications that had to be made to overcome the disadvantages of conventional EM which allowed this reconstruction technique to become more and more popular. Although, the EM algorithm yields just an approximation to the exact solution, physical and statistical factors can be included in the transition matrix [30, Eq. 3] such that better results can be achieved as with FBP, particularly in SPECT. Some of these factors are scatter and attenuation correction and the Poisson nature of the emission process for both SPECT and PET and random coincidence correction in PET only. The ordered subsets expectation maximization (OS-EM) algorithm invented by Hudson and Larkin [22] creates a new image estimate at a fraction of the time required by the conventional EM. It has given ML-EM algorithms their break in clinical practice.

Chapter 3

Attenuation Correction Methods

In section 2.3, the physical phenomena of photon scattering and attenuation in emission tomographic imaging were illustrated. Photon attenuation is believed to be one of the most important causes for image degradation resulting in images in which brightness or counts are not necessarily linear with tracer uptake, thus complicating visual interpretation and quantitative analysis. Reliable correction methods for quantitative emission tomography require accurate delineation of the body contour and often necessitate knowledge of internal anatomic structure especially in inhomogeneous body regions such as the chest [62]. Therefore, these methods try to determine the attenuation map representing the spatial distribution of linear attenuation coefficients.

Zaidi and Hasegawa [62] classified existing attenuation correction methods into two broad classes: transmissionless and transmission-based attenuation correction techniques. Since that, some research groups have been working on new transmissionless approaches. Therefore, a more subtle classification was motivated which led to the underlying structure of this section, to some extent further driven by the more recently by Zaidi et al. [70] published review of strategies for attenuation compensation in neurological PET studies.

Calculated methods which try to determine a uniform attenuation map from the emission data alone are considered at first. Then the to date most commonly used measured methods that require an additional transmission scan, including the CT scan acquired on a dual-modality imaging system, are highlighted, followed by more recently evaluated atlas-based approaches. Methods that make use of a co-registered MR image of the patient to determine the patient-specific attenuation map are considered at last. Few studies have addressed this approach for attenuation correction so far. Particularly against the background of simultaneous PET-MR imaging, MRI-guided approaches will become highly attractive.

3.1 Calculated Methods

Calculated attenuation correction approaches determine the body contour from the emission data alone, which is in general a difficult task. Then, a uniform distribution of linear attenuation coefficients is assigned to the inside of the body, where the magnitude of the attenuation has either to be known, be determined empirically or is based on theoretic assumptions. Hence, calculated attenuation correction is only appropriate for brain studies but more adequate methods must be performed where the attenuation coefficient distribution is not known a priori such as the lungs, where the density varies by as much as 30% [27], and also for areas of inhomogeneous attenuation such as the chest. Therefore, the clinical application of calculated attenuation correction methods was limited to brain studies.

The body contour may either be delineated manually as in the case of the uniform fit-ellipse method [64] or by application of an automatic edge-detection algorithm. Besides the assumption of uniform attenuation, the main limitation of calculated methods is the fact that values for the linear attenuation coefficients of tissues have to be assumed.

Other ambitious and more sophisticated methods, including the application of statistical models for simultaneous estimation of emission and transmission distributions and the application of consistency conditions, which also try to determine the attenuation map directly from the emission data, were summarized by Zaidi et al. [70]. However, the authors reported missing evidence in the literature substantiating the applicability of these techniques in a clinical environment.

3.1.1 Uniform Fit-ellipse Method

The simplest method to derive an attenuation map is to manually draw a slice-dependent ellipse on a preliminary reconstructed emission image to approximate the outline of the head. Then a uniform attenuation is assigned within this elliptical contour. Obvious drawbacks of this method are the operator dependence of the results, the bias due to the poor approximation of the body outline and the assumption of uniform attenuation. An irregular contour can also be drawn by an experienced technologist but requires remarkably more time. Nevertheless, the manual fit-ellipse method is still applied in clinical routine for simplicity reasons, especially when transmission imaging is impractical or even not possible. It is further used by other approaches like the transmission atlas-guided method described in section 3.3.2 to correct a preliminary reconstruction of the emission data.

3.1.2 Automated Contour Detection Methods

To reduce the burden on the operator and to get a better approximation of the outline, automatic edge-detection algorithms are applied [70]. Moreover, the operator dependence of the results is removed by using automated techniques. To account for the considerable higher attenuation of the skull, a higher attenuation coefficient can be assigned within a certain thickness of the outline or by estimating the skull boundary from an emission image reconstructed without attenuation correction. A more sophisticated fully automated technique that works out a three-component model of the attenuation map was proposed by Weinzapfel and Hutchins [57]. This method generates an estimated skull image by FBP of the reciprocal of the emission sinogram. The thickness and radius of the skull are estimated from profiles extracted from this image. The resulting values are then used to generate a model of the brain, skull and scalp. Appropriately scaled linear attenuation coefficients determined empirically are then assigned to each brain structure to generate an attenuation map of the head [70].

3.2 Transmission Methods

Methods that make use of an additional transmission scan, also referred to as measured attenuation correction, are most widely used to date in clinical practice. Clearly, these methods supply more accurate attenuation maps, whereas the patient is subject to additional radiation dose. The transmission scan may either be acquired using an external radionuclide source similar to the radionuclides used in ECT or using a X-ray source as in CT. The latter is especially the case for combined ECT-CT scanners where no additional image fusion has to be performed to co-register the CT image with the emission image. Due to the fact that radionuclide transmission methods rely on mono-energetic photons just as emission imaging, the attenuation maps generated by these are considered as gold standard when comparing different methods for attenuation correction. Whereas radionuclide transmission imaging is still a method widely applied in clinical practice to determine the patient-specific attenuation map, the utilization of CT images has evolved while dual-modality imaging systems became more attention.

3.2.1 Radionuclide Transmission Imaging

In radionuclide transmission imaging in principle an external single-photon or positron emitting source of radiation is placed on one side of the patient and a detector on the other side measures the transmitted photons before (pre-injection), during (post-injection, simultaneously) or after (post-injection, sequentially) emission scanning. The measurements are then compared to the counts of photons observed during a blank scan that is taken, for instance, once each morning when no patient is present in the FOV. Normally, the blank scan is acquired over a long duration and therefore can be assumed as almost free of noise. The ratio of the intensity of the transmission scan to the intensity of the blank scan yields the transmitted fraction as it can be derived from equation (2.4). Logarithmic transformation finally yields:

$$-\ln\left(\frac{I(\theta,t)}{I_0(\theta,t)}\right) = \int_{L(\theta,t)} \mu(x,y)dl, \tag{3.1}$$

where I_0 and I are in particular the sinograms of the blank and transmission scan parametrized over the projection angle θ and the transverse position t and the corresponding projection lines are denoted by L.

Hence, the attenuation map can be reconstructed from the natural logarithm of the blank-to-transmitted sinogram ratios. Iterative reconstruction is preferred, since the Poisson nature of the radioactive decay and random coincidences can be included to get unbiased images with lower variances than by FBP, especially in PET [41, 16]. However, equation (3.1) already yields the ACFs needed in PET if a positron emitting transmission source is used, since the energies of transmission and emission photons are then the same. In this case, no reconstruction of the attenuation map has to take place. In all other cases, the reconstructed linear attenuation coefficients have to be transformed to the photon energy of the emission isotope.

King et al. [26] reported that statistical noise in reconstructed emission images is dominated by the noise in the emission profiles and not the noise in transmission images. The reason for it is that the noise in the attenuation map is averaged out in the process of forward projection to calculate the ACFs. Nevertheless, as the number of counts in transmission profiles decreases, a point is reached where not only does the noise in the attenuation map increase, but the measured attenuation coefficients start to exhibit a bias resulting in an overestimate of the amount of attenuation in the slices on reconstruction. Thus, low transmission counts, cross-talk contributions from the emission isotope, scatter and truncation of the transmission data are the major causes for artifacts in the transmission images, which in turn cause artifacts in the reconstructed emission images as evaluated in SPECT by Celler et al. [9] and in PET by Meikle et al. [35]. Mechanical collimation is required when single-photon emitting transmission sources are used to reduce scatter in the transmission data to get a good estimate of narrow-beam attenuation coefficients.

Transmission imaging is basically performed either pre- or post-injection of the radiopharmaceutical used for emission imaging, where in both cases many approaches have been proposed to reduce the artifacts in the transmission images caused by previously mentioned factors. Some of these approaches are described in more detail in what follows. Several transmission imaging geometries adopted in SPECT were summarized by Zaidi and Hasegawa [62]. Moreover, an overview of different transmission source and collimator configurations used in simultaneous transmission-emission SPECT imaging for single-head and multiple-head systems was given by King et al. [26]. The radionuclide used as transmission source is mainly ^{57}Co, ^{99m}Tc, ^{133}Ba, ^{139}Ce, ^{153}Gd, ^{201}Tl or ^{241}Am depending on the radionuclide used for emission imaging. PET scanners of the second generation typically used one or more continuously rotating rod sources, containing a long-lived isotope such as ^{68}Ge which decays to the positron emitter ^{68}Ga. The transmission scans were commonly be acquired in 2D mode with septa in, whereas most recently single-photon emitting sources are adopted also in PET, allowing for transmission imaging in 3D mode with septa out. Particularly modern PET scanners operate in 3D mode only.

Important drawbacks of radionuclide transmission imaging are the extra complexity of the system design and the data acquisition and processing protocols and the extra cost resulting from the periodic requirement to replace expensive sources [66]. A major limitation of the use of positron-emitting transmission sources in PET, especially in 3D mode, is the high photon flux in the detectors closest to the source, which usually leads to longer scan times because of detector dead time. However, this problem can be relieved by electronic windowing the transmission data so that only events collinear with the known location of the rod are accepted [62].

Pre-injection Radionuclide Transmission Imaging To avoid the contamination of the transmission data, the transmission scan is performed before administration of the radiopharmaceutical. Especially in PET, where a positron emitting source is used for transmission imaging, the separation of both scans, if acquired post-injection, is quite difficult since both transmission and emission photons have the same energies. However, sequential transmission-emission imaging increases imaging time and suffers from image registration problems caused by patient misalignment or motion. The increased acquisition time is especially a handicap in whole-body imaging.

To reduce the acquisition time, short transmission scans of about 2 to 3 min are performed leading to limited transmission counts and consequently higher noise in the transmission images. This is because transmission data undergoes a non-linear transformation before reconstruction as shown in equation (3.1), which introduces singularities and systematic bias. Assuming that the transmission data is corrupted by additive noise n, arising from Compton scatter or random coincidences in PET, the line integrals are given by [41]:

$$\int_{L(\theta,t)} \mu(x,y)dl = -\ln\left(\frac{I(\theta,t) - n(\theta,t)}{I_0(\theta,t)}\right). \tag{3.2}$$

Since the logarithm is only defined for positive numbers, the line integrals do not exist for zero or negative values of the numerator on the right side of equation (3.2). Moreover, the logarithm skews the distribution of the line integrals for low-count data such that the estimated integrals are biased. Therefore, the integrals are undefined for some projections and biased for others [41].

One way to reduce noise in the transmission data is the segmented attenuation correction (SAC) approach proposed by Xu et al. [58]. The reconstructed transmission image pixels are segmented into populations of uniform attenuation. The resulting distribution of linear attenuation coefficients is then forward projected to get new ACFs. This reduces noise in ACFs while still accounting for specific areas of differing attenuation. The majority of segmentation methods

used are either histogram-based thresholding techniques or fuzzy-clustering-based segmentation techniques. Whereas the performance of the first techniques depends strongly on the choice of thresholds, techniques of the last category demonstrated excellent performance and produced good results as an automated, unsupervised tool for segmenting noisy images in a robust manner [62, 70]. A method based on the fuzzy C-means (FCM) algorithm, for instance, was presented by Zaidi et al. [61]. Meikle et al. [35] investigated the influence of count-limited transmission data on the noise and quantitative accuracy of reconstructed images in PET and concluded that accurate attenuation correction can still be performed if SAC methods are applied.

Other approaches to reduce noise in transmission images include non-linear Gaussian filtering as evaluated by Kitamura et al. [29], anisotropic diffusion filtering as investigated by Demirkaya [11] and iterative reconstruction algorithms as the ML-EM algorithms [41, 16] and the median root prior iterative reconstruction method proposed by Alenius et al. [1]. An advantage of the iterative reconstruction methods is that they are object independent and robust, because no smoothing or segmentation is used. On the other hand, calculation time is longer especially in the case of whole-body studies.

As mentioned before, coincidence transmission imaging with positron emitting rod sources in PET suffers from poor SNR due to low counts resulting from losses caused by dead time of mainly the detectors on the near side. A first prototype single photon transmission measurement method was implemented and evaluated by de Kemp and Nahmias [12]. This method removed the coincidence requirement and adopted the singles events of annihilation photons to get the transmission image, whereby SNR could be dramatically increased. The feasibility of using right single-photon emitting transmission sources of energy other than the one of the annihilation photons in PET was investigated almost at the same time by Karp et al. [25] and Yu and Nahmias [60]. The authors of both suggested to use ^{137}Cs with a photon energy of 662 keV and a half-life of 30.2 y as transmission source, which has low costs compared to the commonly used ^{68}Ge rod sources and needs no replacement due to its long half-life compared to ^{68}Ge/^{68}Ga with a half-life of about 275 d. Moreover, it has the potential to be used in post-injection transmission imaging with energy discrimination to separate the transmission from emission data. One significant advantage of single-photon transmission imaging in PET is that a stronger source can be used without saturating the system. As a result, a very high photon flux is recorded, which leads to high-quality scans compared to coincidence measurements and a remarkably reduction of acquisition time. However, post-processing of the data to transform the measurements to the energy of the annihilation photons and, even with a narrow energy window, additional scatter compensation are required.

Post-injection Radionuclide Transmission Imaging To reduce the overall acquisition time, the transmission scan is performed after administration of the radiopharmaceutical such that even simultaneous transmission-emission imaging is possible. This has proven to be very practical especially in whole-body oncology studies in which multiple bed positions are needed. However, cross-talk between transmission and emission measurements has to be obstructed.

Properties a radionuclide for simultaneous transmission-emission imaging in SPECT should have were given by King et al. [26]. The ideal radionuclide would emit mono-energetic photons of energy lower than those of the emission source to avoid cross-contamination. On the other hand, it would emit photons of energy close enough to reduce the magnitude of the correction required to convert the attenuation map measured at the transmission photons' energy to that of the emission photons. Furthermore, it would have a long half-life so that the transmission source will require replacement infrequently and last, it would not be expensive to manufacture. Given these requirements, ^{153}Gd, for example, is a good choice to use as transmission source for in SPECT commonly used pharmaceuticals labeled with ^{99m}Tc [26].

Amongst all possible configurations of transmission imaging geometries in SPECT, the scanning line source with parallel-hole collimation and electronic windowing to store only the events detected in a narrow region opposed to the line source and a stationary line source with convergent fan beam collimation have attained widespread use. Whereas the advantages of the convergent collimation are that no mechanical motion is required and that it provides a better spatial resolution sensitivity combination for small structures such as the heart, the disadvantages are that the line source has to be fixed at the focal point of the collimator and the increased truncation of the FOV. However, both methods measure near narrow-beam attenuation coefficients and moreover reduce greatly the influence of cross-contamination.

Meikle et al. [36] proposed a methodology for attenuation correction in whole-body PET using simultaneous emission and transmission measurements (SET). The SET method employs sinogram windowing of low activity ^{68}Ge/^{68}Ga rod sources, an SAC approach and ML-EM reconstruction using the OS-EM algorithm. The sinogram windowing technique continuously encodes the angular displacement of one or more rod sources rotating about the center of the FOV, enabling the determination of sinogram elements representing collinear detector pairs. Coincidences recorded within a narrow window centered on each rod are stored in a seperate sinogram of primarily transmission events from those primarily emission events recorded outside the window. However, some coincidences spill over into the other window at a time. Fortunately, the spillover fraction is constant and depends only on the width of the sinogram window, but not on the emission source distribution and geometry. The SAC approach used by Meikle et al. ap-

proximates the whole-body histogram of the ACFs by Gaussian functions about the lung and soft tissue peaks. Then, cumulative probability density functions are calculated for each peak by integrating under the fitted curve, which are then used to calculate for each pixel the probabilities that it belongs to lung or soft tissue. New attenuation coefficients are calculated as the by the probabilities weighted sum of known attenuation coefficients for lung and soft tissue.

Since, as mentioned before, single-photon transmission imaging has been shown to be feasible also in PET, simultaneous acquisition was offered by transmission sources that emit photons of energy different from that of the annihilation photons. A clinical evaluation of single-photon attenuation correction using ^{137}Cs for 3D whole-body PET was first accomplished by Watson et al. [56]. The authors concluded, that, at least with the protocol they used, high emission background is not a significant problem in post-injection transmission imaging and that such attenuation corrected emission images are acceptable for clinical use in most cases.

3.2.2 X-ray Transmission Imaging

X-ray-based transmission imaging is conceptually identical to single-photon-based or positron-based transmission imaging as described in the previous section on radionuclide transmission imaging. Since in CT photon attenuation governs image contrast, pixel values contained in CT images are related to the attenuation coefficient at that point. Hence, it is not surprising that CT can generate patient-specific attenuation maps as well. The CT image may either be acquired separately and then co-registered with the emission image or better and more commonly acquired sequentially on a dual-modality scanner, thus already co-registered with the emission data.

An advantage of CT-based attenuation correction are the high resolution transmission images with much lower statistical noise than in standard transmission imaging. Nevertheless, the high-resolution CT images are usually down-sampled and Gaussian filtered to match the resolution of the emission data. Further advantages are the shorter times required for collecting the transmission data, which improves patient comfort and throughput, and that it is no longer necessary to include radionuclide transmission sources, thus eliminating both the cost of including these components and the periodic replacement of decayed sources [27].

However, opposed to the mono-energetic photons emitted by the radionuclides, the X-ray source in CT emits photons which cover a relatively broad energy spectrum from 20 to 140 keV. Moreover, the attenuation at these energies is a combination of both photoelectric effect and Compton scattering, whereas at the emission photons' energy in ECT the contribution of photoelectric effect is essentially negligable [4]. Hence, the CT images have to be energy-translated to an accurate attenuation map at the emission radionuclide energy, where the measured attenuation coefficients in CT correspond to the attenuation at the effective CT energy. The effective CT energy is defined as that photon energy at which a given material will exhibit the same attenuation coefficient as it is measured by CT. However, for a propagating X-ray beam, the low energy photons are preferentially absorbed, so that the remaining beam becomes proportionately richer in high energy photons. This phenomenon is called beam hardening [24]. Consequently, the actual effective energy may vary spatially. Pixel values in reconstructed CT images are scaled as Hounsfield units (HU), named after Godfrey Hounsfield [24]:

$$H := 1000 \left(\frac{\mu^{\mathrm{CT}}}{\mu^{\mathrm{CT}}_{\mathrm{water}}} - 1 \right), \tag{3.3}$$

where H is the CT number in HU, μ^{CT} is the reconstructed linear attenuation coefficient and $\mu^{\mathrm{CT}}_{\mathrm{water}}$ is the estimated linear attenuation coefficient of water at the effective CT energy.

In this scale, air has the value -1000, water has the value zero, and tissues denser than water have values greater than zero. CT numbers in the range of -1000 to zero primarily represent regions that contain mixtures of lung and soft tissue, whereas regions having CT numbers greater than zero are those that contain mixtures of soft tissue and bone. Compact bone typically has values in the range from 1000 to 2000, whereas adipose tissue has values near -100 [28].

Unfortunately, there is no unique transformation from CT energies to the emission photon energy when the object contains a complex mixture of material components such as CT contrast agents or metallic objects. Errors can also arise from respiratory motion, truncation of the FOV in CT, and beam-hardening or scattered radiation if the patient's arms are in the FOV of the CT scan [28]. A summary of pitfalls of CT-based attenuation correction in PET and potential solutions was just recently published by Zaidi et al. [69].

Basically five methods have been proposed to obtain attenuation coefficients at the emission photon energy from CT images: segmentation, uniform scaling, bilinear scaling, hybrid segmentation/scaling and dual-energy decomposition.

Segmentation This method forms the attenuation map by segmentation of the reconstructed CT image into different regions such as soft tissue, bone and lung and then substitution of the CT numbers in each region with the appropriate attenuation coefficients. A significant problem is that any errors in segmentation can lead to artifacts in the reconstruction of the attenuation corrected data. Furthermore, certain tissue regions will have densities that are not accurately represented by a discrete set of segmented values such as, for example, the lungs, where the density can easily vary by as much as 30%. Such segmentation errors will affect all LORs passing through the misclassified region which can lead to the generation of artifacts when applied to the emission data [4]. However, Kinahan et al. [27] reported that the segmentation method produced good results and that an alternative segmentation method has been proposed by Xu et al. [59] which has proven to be robust even in areas of gradually changing tissue density. This method combines tissue classification and measured values, however, so it cannot be used directly.

Uniform Scaling The simplest method is to scale the measured attenuation coefficients by a global scaling factor using the fact, that, for most materials, the ratio of the attenuation coefficient at any two photon energies is essentially a constant. The ratio of attenuation for water at the emission photon energy and the effective CT energy yields the scaling factor. Before, the CT numbers must be translated back to linear attenuation coefficients according to equation (3.3). All in all, the energy-translated attenuation coefficient using uniform scaling is given by [33]:

$$\mu = \mu_{\text{water}}^{\text{CT}} \, \frac{H + 1000}{1000} \times \frac{\mu_{\text{water}}}{\mu_{\text{water}}^{\text{CT}}} = \mu_{\text{water}} \, \frac{H + 1000}{1000} \, , \tag{3.4}$$

where μ_{water} is the theoretic attenuation coefficient of water at the emission photon energy.

This linear translation method provides a good approximation for scaling between photon energies where Compton interactions dominate the attenuation coefficient, but is not as accurate when scaling from lower photon energies, commonly found in X-ray spectra, where photoelectric interactions significantly contribute to the attenuation coefficient. The error is particularly large for higher Z materials such as bone, which contains a relatively large percentage of calcium, and so has a significantly higher photoelectric fraction than water in the range of CT energies. Moreover, the error is even larger in PET than in SPECT since the energy of the annihilation photons in PET is 511 keV, whereas in SPECT the emission photon energy is typically in the range of 100 to 200 keV. Thus, the resulting attenuation maps accurately estimate the attenuation coefficients for both muscle and lung tissues, but not for bone tissues [33, 4].

Bilinear Scaling Instead of just applying a linear translation, Blankespoor et al. [5] derived a piecewise linear function for SPECT at 140 keV. Therefore, a phantom study with calibration materials, particularly air, water and bone-equivalent solutions, has been performed. Then a piecewise linear calibration curve was obtained from this study, which was more precisely a bilinear function with a change in slope at the CT number of water. This method can be considered as combining an air/water mixture model for -1000 $< H \leq 0$ and a water/bone mixture model for $H > 0$ [28].

Burger et al. [7] evaluated a transformation of CT into PET attenuation coefficients that uses the bilinear function:

$$\mu = \begin{cases} \mu_{\text{water}} \, \frac{H+1000}{1000}, & H \leq 0 \\ \mu_{\text{water}} + H \, \frac{\mu_{\text{water}}^{\text{CT}}(\mu_{\text{bone}} - \mu_{\text{water}})}{1000(\mu_{\text{bone}}^{\text{CT}} - \mu_{\text{water}}^{\text{CT}})}, & H > 0 \end{cases}, \tag{3.5}$$

where the linear attenuation coefficients were estimated at an effective energy of the X-ray spectrum of 80 keV and the energy of the PET annihilation photons of 511 keV. Particulary, the linear narrow-beam attenuation coefficients used for the transformation of CT into PET attenuation coefficients were:

$$\begin{aligned} \mu_{\text{water}} &= 0.096 \text{ cm}^{-1} \\ \mu_{\text{bone}} &= 0.172 \text{ cm}^{-1} \\ \mu_{\text{water}}^{\text{CT}} &= 0.184 \text{ cm}^{-1} \\ \mu_{\text{bone}}^{\text{CT}} &= 0.428 \text{ cm}^{-1} . \end{aligned} \tag{3.6}$$

However, the authors reported that using for μ_{water} the theoretic narrow-beam value of 0.096 cm^{-1} for the transformation resulted in an obvious discrepancy in the range of 0 to 200 HU. Therefore, the transformation was modified to be based on the experimentally determined value of 0.093 cm^{-1} that was measured with a phantom.

The same bilinear function was mentioned in an only recently published article of Patton and Turkington [42] for SPECT. Although the formulas printed in the article are incorrect, it is clear, however, that the authors indeed used the bilinear function given by equation (3.5) with the theoretic linear attenuation coefficients at the PET annihilation photon energy appropriately substituted with the linear attenuation coefficients at the SPECT emission photon energy.

Hybrid Segmentation/Scaling Another straightforward solution that combines the segmentation and uniform scaling approaches to overcome the difference in ratios of attenuation coefficients at any two energies for bone and non-bone tissues is to just segment the bone component of the CT image and to scale it differently. This hybrid method was proposed by Beyer et al. [4] for PET and later evaluated by the same authors in [27] where the segmentation is carried out by simple thresholding. The hybrid method is unlike the bilinear method not piecewise continuous, since the change in scaling factors leads to a discontinuity at the threshold value. Nevertheless, both the bilinear and hybrid scaling methods work well for clinical procedures where only biological materials are being imaged [28].

Dual-energy Decomposition In dual-energy decomposition, the CT image is acquired at two different effective photon energies and these data is then used to extract the individual photoelectric and Compton contributions to the attenuation coefficient. The different contributions can then be scaled separately in energy and combined to form a mono-energetic attenuation map at any emission photon energy [4]. The dual-energy decomposition can theoretically produce an attenuation map which accurately estimates the attenuation coefficients of all tissues, including bone, and is free from beam hardening artifacts. However, whether using an energy-discriminating detector or a conventional CT scanner for data collection, dual energy measurements are, in general, more difficult and time-consuming to obtain. Furthermore, the X-ray beams must be highly filtered so that there is minimal energy overlap of the high and low energy beams. Moreover, dual-energy CT applies more radiation dose to the patient [33]. To overcome the potential time penalties and to reduce both costs and patient dose, Guy et al.[18] designed an acquisition protocol where the beam energy is switched between alternate slices, producing two interleaved attenuation maps and allowing two complete attenuation maps at different effective CT energies to be obtained from one CT scan. The authors referred to their method as Dual Energy Transmission Estimation CT (DETECT).

3.3 Atlas Methods

Atlas-based methods try to derive the patient-specific attenuation map from an inferred atlas of attenuation coefficients scaled to the appropriate photon energy. The main idea behind these approaches is to obtain the attenuation map by anatomic standardization, which warps the atlas image such that the result can be considered as being a measurement of the spatial distribution of linear attenuation coefficients of the examined patient.

Montandon and Zaidi [38] emphasized the conceptual difference between anatomic standardization, also called spatial normalization, and co-registration. Basically, co-registration aims to match images of a single subject, usually of a different tracer or modality, through rigid or non-rigid transformation. Contrary, the purpose of anatomic standardization is to transform images of individual subjects into a standard, for instance a standard brain. Another important difference is that a true solution exists for registration but not for anatomic standardization. Standardization therefore has to be performed with caution. Nevertheless, co-registration and spatial normalization are the same from a mathematical point of view and thus seldomly explicitly distinguished.

A rather important conceptual limitation of the approaches presented here is that existing patient-specific anomalies cannot be modeled in an atlas obtained from a single or even an average representation of the population [38].

3.3.1 Inferring-attenuation Distributions Method

The method of inferring-attenuation distributions (IAD) was developed by Stodilka et al. [53] to correct brain SPECT images for photon scatter and attenuation. The motivation of the method was that neurologically impaired patients are unable to keep their head motionless for the extended duration of sequential emission and transmission scans. Thus, an alternative method that does not require an additional transmission scan had to be invented.

IAD is based on the assumption that a transformation mapping analogous features from two SPECT scans of different subjects into the same spatial coordinates would also register the two corresponding transmission scans [53]. The head atlas used was derived from the Zubal head phantom, a digitized high-resolution head phantom of a single subject. This phantom was segmented to produce a tracer-specific SPECT atlas that consists of voxels containing only the brain component, simulating a SPECT scan of the phantom. Furthermore, an anatomic atlas was generated assigning appropriate attenuation coefficients to the voxels of this atlas, simulating a transmission scan of the phantom. Both SPECT and anatomic atlases build the functional and anatomic component of the head atlas. The functional component of the head atlas is deformably

registered to a preliminary reconstruction of the patient SPECT scan and the spatial transformation is recorded. Then, the patient's anatomy is inferred by the anatomic component of the head atlas. This technique was later also extended and implemented for brain PET imaging as reported by Zaidi et al. [70].

One drawback of the method is that the applied transformation is restricted to seven parameters for rotation, translation and global scaling. Better results have been achieved using a non-linear warping algorithm instead [64]. Further does the registration rely on the assumption that the spatial distribution of radioactivity is representative of the underlying anatomy [53]. A limitation of the Zubal head phantom is that the sinus appears to be larger than usual [53, 64] and new phantom models based on average patient populations may not help to solve this problem owing to the large variability in size and shape of the frontal sinus among patients as noted in [64]. However, Stodilka et al. evaluated that SPECT reconstructions guided by IAD are sufficiently accurate to identify regional cerebral blood flow deficits of 10%, which are typical in moderate and advanced dementia.

3.3.2 Transmission Atlas-guided Method

An extension to the previously described IAD approach was proposed recently by Montandon and Zaidi [38]. One of the improvements to yield more robustness was to construct the transmission and tracer-specific emission atlases based on average patient populations rather than a single subject. Thus, also eliminating the reliance on the hypothetical tracer distribution. The second improvement is the use of a non-linear warping algorithm instead of just a simple global rescaling procedure as also already suggested in [64]. In contrary to the non-corrected preliminary reconstruction of the emission image, a model-based scatter correction and uniform fit-ellipse based calculated attenuation compensation were performed before the preliminary reconstruction step to improve registration accuracy [53, 38], whereupon the algorithm performance strongly depends as the registration is the crucial step which is in common with all atlas-based methods.

Montandon and Zaidi also assessed the quantitative accuracy of the method for 3D brain PET in [39] using automated volume of interest-based analysis. They reported a very good correlation between the atlas-guided and measured transmission-guided attenuation correction techniques. Nevertheless, relevant issues include the effect of abnormal anatomy and/or uptake in patients as well as the relevance of building tracer-specific templates to allow application of the proposed algorithm for children and other tracers. The authors envisaged the use of cost-function masking to exclude abnormal anatomy or uptake during the normalization procedure.

3.4 Magnetic Resonance Imaging Methods

The goal of MRI-guided attenuation correction methods is to derive the attenuation map from an MR image of the patient whose emission data is to be corrected. Therefore, the MR image has to be aligned in any way to a preliminary reconstructed emission image as it is also the case for atlas-based methods. However, a already co-registered MR image will be available once a combined PET-MR scanner is on the market. By then, methods within this category of attenuation correction strategies have to deal with the problem of separately acquired MR images. But the actual difficulty is to find a mapping between the non-standardized, by means of magnetic field inhomogeneities distorted intensity values and the appropriate energy-dependent linear attenuation coefficients. Thus, few publications addressed this type of approach so far and none of them yet produces unconditionally satisfying results, especially in whole-body ECT. The latest methods adapt atlas-based approaches and could also be classified as atlas-based methods, however, an MRI acquisition is employed to guide the determination of the attenuation map, whereas plain atlas-based methods do not require an additional acquisition besides ECT.

3.4.1 Segmented Magnetic Resonance Imaging Method

Zaidi et al. [63] developed an approach to derive the attenuation map from a segmentation of a co-registered MR image. The authors aimed in general to investigate the feasibility of segmented MRI-guided scatter and attenuation correction. To simulate combined ECT-MRI, the brain component of the MR image is extracted and is realigned to a preliminary reconstruction of the emission data using an automatic algorithm. Since it has been shown that scatter and attenuation correction of the preliminary reconstructed emission data improves registration, a model-based scatter correction and calculated uniform fit-ellipse method are performed before the preliminary reconstruction. The recorded spatial transformation is then applied to the original MR image. Then, to determine the attenuation map, the MR image is segmented into five regions of air, brain tissue, skull, nasal sinuses and scalp by means of a fuzzy clustering segmentation, in particular a FCM algorithm, where a contour detection algorithm is used to identify the external boundary of the head. Because brain and scalp tissue have the same attenuation properties, they are merged afterwards. Appropriate attenuation coefficients are now assigned to the four remaining regions followed by Gaussian smoothing to approximate the resolution of the ECT scanner, resulting in the final MRI-guided patient-specific attenuation map. An attenuation map-guided scatter correction using the single-scatter simulation technique is performed, prior to the non-uniform attenuation correction and the final reconstruction of the emission data.

Such as CT-based attenuation correction using segmentation, the segmented MRI method has the problem that any errors in segmentation can lead to artifacts in the reconstruction from the attenuation corrected data. The authors indeed reported that the difficulties associated with automatic segmentation of the skull on the T1-weighted spin-echo images using the FCM algorithm led to some manual intervention of the operator. This intervention consisted in filling the complexly shaped skull base using a morphological closing operation to make it more uniform. Since the FCM algorithm does not place any contextual constraints on the membership functions, excessive noise and other artifacts such as intensity inhomogeneities that are not unlikely in MRI may obstruct the segmentation. Furthermore, certain tissue regions will have densities that are not accurately represented by a discrete set of segmented values. Additionally, the attenuation of the classified tissues has to be assumed. Another very important drawback of segmented MRI is that some anatomy may be missed by MRI, as, for example, both bone compacta and air do not contribute a MR signal whereas their attenuation coefficients are maximally distinct [20]. Notwithstanding, the authors reported results that indicate a small but noticeable improvement in image quality as a consequence of the reduction of noise propagation from transmission to emission data. But it has also be noted that these results are restricted to brain PET imaging and the amplification for whole-body PET imaging has yet to be investigated.

3.4.2 Nuclear-medical Magnetic Resonance Atlas Method

Krieg et al. [31] developed a method that adapts the idea of atlas-based methods to an MRI-guided approach. An atlas with a reference MR image and a corresponding correction data set, entitled nuclear-medical magnetic resonance (NM-MR) atlas, is generated and provided for attenuation correction of the emission data. The information required for attenuation correction is present, for example, in the form of attenuation coefficients due to the correction data set. The data points of the reference MR image are either associated directly with data points of the correction data set or indirectly with values of the correction data set via the assigned MR intensities. For the first purpose, the reference MR image and the correction data set are stored in a common matrix. For the second purpose, the reference MR intensities are classified into the most probable tissue types and known attenuation coefficients are associated with the intensity intervals of classified tissue types. The determination of the patient-specific attenuation map is carried out in two steps, where the MR image of the patient is assumed to be co-registered with the emission data. First, the reference MR image of the NM-MR atlas is registered with the MR image of the patient and the transformation is recorded. Then, the recorded transformation is applied to the correction data set yielding the attenuation map used for attenuation correction

in case that the correction data set consists of appropriate attenuation coefficients. Compared to the atlas-based methods described in the previous section, the NM-MR atlas-based method generally just substitutes the registration of the atlas with a preliminary reconstruction of the emission image with a registration of the reference MR image with the co-registered MR image of the patient. However, this difference has an important impact on the registration accuracy that can be achieved, as an intramodality instead of intermodality registration is employed, where both images to be registered image the same type of information.

Chapter 4

Magnetic Resonance Imaging-guided Computed Tomography Prediction Method

The combination of PET with MRI instead of CT is currently in progress while first brain images have yet been published, demonstrating the feasibility of this technological evolution [50]. However, it has also been emphasized that a major issue is the derivation of an accurate non-uniform attenuation map from the simultaneously acquired MR image. Recently, Zaidi [65] occupied himself with the question if MRI-guided attenuation correction is a viable option for dual-modality PET-MR imaging, where he outlined the difficulties associated with such an approach. The major difficulty lies in the fact that the MR signal or tissue intensity level is not directly related to electronic attenuation, which renders conversion of MR images to attenuation maps less obvious. Moreover, pixel values in MRI are not normalized as is the case in CT, where Hounsfield units determine different tissue types. In MRI, different types of tissues can have identical signal intensities and similar types of tissue can have different signal intensities. In addition, signal intensity varies strongly between MR images. On the other hand, transmission imaging is no choice for PET-MRI because of the limited space available, thus, circumventing the placement of external radionuclide sources. Beneath the few already proposed MRI-guided attenuation correction approaches, little convincing results have been achieved so far.

The evaluated CT atlas-based approach to determine the attenuation map guided by MRI is presented in this chapter, moreover, it is related to other proposed approaches where reasonable. At first the basic concept of the approach is explained. Afterwards, both major steps, first to predict a CT image from the MR image of the patient, second to translate the CT image to a patient-specific attenuation map, are described in detail. At last follows a brief recapitulation of the compensation for photon scatter and attenuation during reconstruction.

4.1 Overview

The idea of the presented approach to determine the attenuation map from a co-registered MR image is quite straightforward and can be viewed as a combination of different already proposed attenuation correction methods or the application of CT-MR registration followed by any CT-based technique. However, as usual, the difficulties are hidden in the details that have to be solved to come up with a practical working solution, eventually. The flow of data and the steps deployed to determine the attenuation map at the emission photon energy from the patient's MR image are summarized in Figure 4.1. In a first step, an approximation of a X-ray transmission scan of the patient is predicted using the anatomical information provided by MRI. This step applies deformable CT-MR registration and makes use of a CT atlas. Then the patient's attenuation map at the emission photon energy is determined applying well-known CT-based techniques. After the attenuation map is available, it can be incorporated in the reconstruction of the emission data to compensate for scatter and attenuation.

Since methods are yet being successfully applied which determine the attenuation map from a CT image, the second step of generating the attenuation map at the emission photons' energy from the predicted CT image does not pose a problem. Hence, the main step whose feasibility and robustness has to be investigated is the CT prediction step.

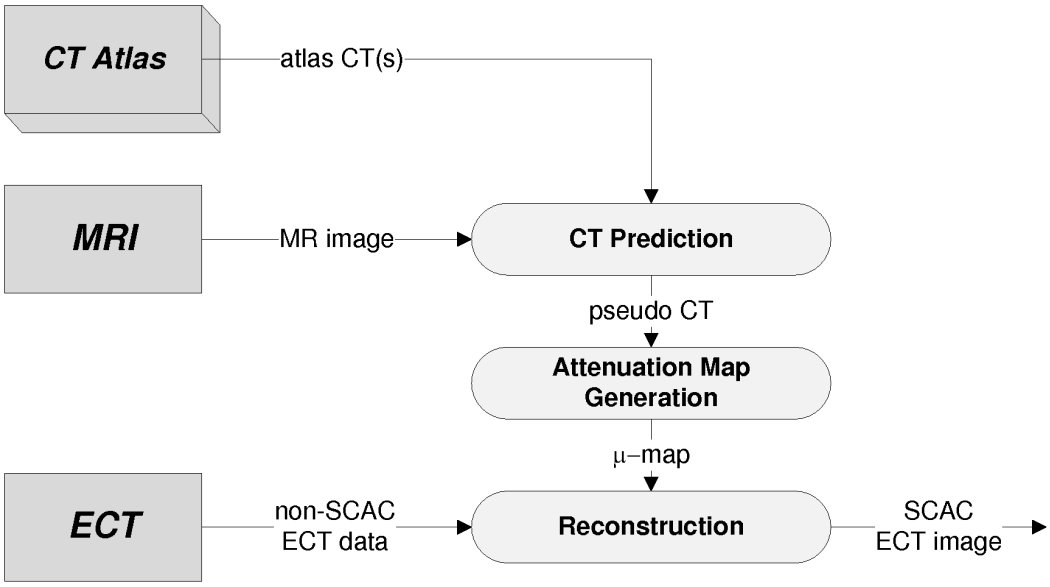

Figure 4.1: Compact flow chart of the MRI-guided CT prediction method

4.2 Computed Tomography Prediction

The anatomical information contained in the MR image is used to predict a CT of the patient. Deformable CT-MR registration is applied to infer CT numbers from a suitable CT image provided by an atlas, optionally pre-selected from a set of reference CTs. The resulting CT image is considered as a prediction of a X-ray transmission scan of the patient pictured by MRI that is scaled at Hounsfield units and is referred to as pseudo CT. The corresponding flow chart expanded on the prediction of the pseudo CT is given by Figure 4.2.

The used terminology already implies the relation to the IAD method proposed by Stodilka et al. [53], that was more recently extended by Montandon and Zaidi [38]. In contrast, a CT atlas is used and the attenuation distribution is inferred using a spatial transformation obtained by CT-MR instead of atlas-ECT registration, which is more robust due to the registration of anatomical images only. Registration of anatomical and functional images may be difficult, as the functional image may provide insufficient anatomy. Moreover, the method introduced in this chapter is quite similar to the method proposed by Krieg et al. [31], with the correction data set consisting of proper CT numbers. Again, the actual difference is the determination of the transformation, which is accomplished indirectly by Krieg et al. using intramodality registration but directly by the investigated method using intermodality registration.

4.2.1 X-ray Transmission Atlas

The foundation of the CT prediction is a reliable atlas from which an appropriate CT image can be attained that ideally would correlate with the unknown patient-specific spatial distribution of CT numbers. Clearly, a global atlas will almost never meet this ideal situation, however, the atlas can provide CT images which are common for human beings. Basically two types of CT atlases suggest themselves: An atlas consisting of only one representative average CT or an atlas composed of a whole set of average CTs each representative for just a specific subgroup. An advantage of the latter is that it may also contain average CTs imaging abnormalities ordinary for different diseases. Moreover, the set of CT images should maintain combinations of opposing features like child and grown-up, skinny and plump, male and female, especially in regions where it makes appreciable difference such as the thorax and pelvis. On the other hand, a complex atlas composed of a set of CTs requires more disk space and more importantly does it require an appropriate template selection strategy on the basis of the patient's MR image that utilizes pattern classification. This classification increases the complexity even more and may also increase the sensitivity of the CT prediction. However, an operator could pre-select a suitable subset.

4.2.2 Deformable Registration

To infer the spatial distribution of CT numbers, a deformable CT-MR registration, in particular non-parametric registration following rigid pre-registration, is suggested. The mathematical setting of such a deformable registration and numerical schemes to solve this kind of mathematical problem were given by Modersitzki [37] in his extensive and mathematical precisely phrased book on numerical methods for image registration. The pre-registration can be carried out manually and/or automatically, where the transformation is restricted to translation and rotation only. In this section, the required mathematical setting used by Modersitzki is first re-considered, followed by the general mathematical framework of the non-parametric registration problem. Afterwards, the distance measure commonly used for automatic intermodality registration and the recommended regularization of the non-parametric registration are discussed.

Mathematical Setting According to Modersitzki [37, ch. 3.1], in the following an image b is viewed as a mapping which assigns each spatial location $\boldsymbol{x}$ belonging to a certain domain $\boldsymbol{\Omega} \subset \mathbb{R}^3$ a gray value $b(\boldsymbol{x}) \in \mathbb{R}$. Furthermore, the function b has the following properties:

1. b is compactly supported,
2. $0 \leq b(\boldsymbol{x}) < \infty$ for all $\boldsymbol{x} \in \mathbb{R}^3$ and
3. $\int_{\mathbb{R}^3} b(\boldsymbol{x})^k dx$ is finite for $k > 0$.

As an image is digitalized, which means that intensities are discrete and given on a discrete grid only, an appropriate interpolation scheme has to be chosen that provides interpolated intensity values for non-grid points, too. The interpolation scheme is mostly based on linear interpolation and has to avoid interpolation artifacts which were investigated by Pluim et al. [44].

Considering the registration problem, cf. [37, ch. 3.3 and 8], a reference R and a template T are given and a spatial transformation $\boldsymbol{\varphi}$ is searched such that the deformed template $T_{\boldsymbol{\varphi}}$, where $T_{\boldsymbol{\varphi}}(\boldsymbol{x}) := T \circ \boldsymbol{\varphi}(\boldsymbol{x})$, is as similar as possible to the reference R according to the similarity measure used. In the case of non-parametric registration the transformation $\boldsymbol{\varphi}$ can be written as:

$$\boldsymbol{\varphi}(\boldsymbol{x}) = \boldsymbol{x} - \boldsymbol{u}(\boldsymbol{x}) \,, \tag{4.1}$$

where $\boldsymbol{u} : \mathbb{R}^3 \rightarrow \mathbb{R}^3$ is the so-called deformation or displacement field. Consequently, for readability reasons, the by the deformation $\boldsymbol{u}$ deformed template T is denoted as:

$$T_{\boldsymbol{u}}(\boldsymbol{x}) := T(\boldsymbol{x} - \boldsymbol{u}(\boldsymbol{x})) \,. \tag{4.2}$$

Variational Formulation A direct minimization of a suitable distance measure D is not possible since this problem is ill-posed, which means that small changes of the input data may lead to large changes of the output data. Moreover, as the problem is not convex, no unique solution exists and the deformation may not even be continuous. The remedy is to impose implicit assumptions on the transformation and thus to come up with an appropriate measure both for the similarity of the images as well as for the likelihood of a non-parametric transformation. Therefore, a regularizing term or smoother S is introduced which makes it possible to distinguish particular transformations which seem to be more likely than others. So, the variational formulation of the non-parametric registration problem is given by [37, Problem 8.1]:

$$\hat{\boldsymbol{u}} = \arg\min_{\boldsymbol{u}} J[\boldsymbol{u}] \;, \tag{4.3}$$

where J is a functional defined as:

$$J[\boldsymbol{u}] := D[R, T_{\boldsymbol{u}}] + \alpha S[\boldsymbol{u}] \;. \tag{4.4}$$

The distance measure D can be viewed as the driving force of the registration, whereas the regularizer controls the transformation. Moreover, the parameter $\alpha \in \mathbb{R}^+$ weights the regularizing term relative to the distance measure or, in other words, depicts the amount of regularization.

A necessary condition for a minimizer $\hat{\boldsymbol{u}}$ of the problem given by equation (4.3) is that the Gâteaux derivative $\mathrm{d}J[\hat{\boldsymbol{u}}; \boldsymbol{v}]$ of J, also known as the first variation of J in the direction of $\boldsymbol{v}$, vanishes for all suitable perturbations $\boldsymbol{v}$. The stated condition leads to the corresponding Euler-Lagrange equations and finally to a system of non-linear partial differential equations.

Entropy The distance measure commonly used for automatic intermodality registration is nowadays mutual information. This distance measure is based on entropy, which itself has been used as distance measure as well. Hartley first introduced such an entropy, a measure for the information of a message with s different possibilities for each symbol that increases linearly with the length n of a message and that depends on the number of possible messages s^n [45]:

$$H := \log s^n = n \log s \;. \tag{4.5}$$

The larger the number of possible messages, the larger the amount of information to get from a certain message. If only a single message is possible, no information can be gained by receiving this message, since it was already known that this is the only one which could be received. In this respect, the measure can be viewed as a measure of uncertainty.

Later on, Shannon introduced an entropy that also minds that different symbols may have different probabilities to occur. Hence, he weighted the information per outcome by the probability of that outcome occuring. The established Shannon entropy is defined as [45]:

$$H := \sum_{i=1}^{m} p_i \log \frac{1}{p_i} = -\sum_{i=1}^{m} p_i \log p_i \ , \tag{4.6}$$

where m is the number of possible events and the term $\frac{1}{p_i}$ inversly relates the information gained from an event to the propability p_i that it takes place. The more rare an event, the more meaning is assigned to the occurence of the event. When all messages are equally likely, the entropy is maximal, because it is completely uncertain which message will be received. Shannon's entropy is the average amount of information to be gained from a certain set of events.

In the case of an image A, the Shannon entropy:

$$H(A) := -\int_{-\infty}^{\infty} p_A(a) \log p_A(a) da \ , \tag{4.7}$$

is a measure of dispersion of p_A, the density of the intensity values a. The density of an image's intensities can be estimated from the histogram of its discrete representation, which counts the times of occurence of each intensity value. Dividing each histogram entry by the total number of pixels results in the discrete probability distribution of the intensities. The density function of these can then be estimated applying non-parametric density estimation techniques as the Parzen window method with a Gaussian window function as described for instance in [14, ch. 4.3]. A density with a single sharp peak corresponds to a low entropy value, whereas a dispersed density yields a high entropy value.

The entropy of the joint density estimated from the joint histogram of two images, in turn calculated for the overlapping parts of the images, can be used to measure the degree of registration, as the joint histogram shows more dispersion while the images are worse registered and vice versa. The joint entropy of two images is defined as [45]:

$$H(A, B) := -\int_{-\infty}^{\infty} \int_{-\infty}^{\infty} p_{A,B}(a, b) \log p_{A,B}(a, b) da db \ , \tag{4.8}$$

where a and b are the intensity values in image A and image B, respectively. If the joint entropy is minimal, then the two images should be registered [45].

Mutual Information Since the joint entropy is computed for the overlapping parts of the images, it is sensitive to the size and the contents of the overlap. A problem that can occur when using joint entropy as distance measure is that low values can be found for complete misregistrations, for example when only background overlaps. Mutual information tries to avoid this problem by including the marginal entropies [45]:

$$MI(A, B) := H(A) + H(B) - H(A, B) \, . \tag{4.9}$$

The marginal entropies will have higher values if the images contain structures such as anatomy, and low values for background only. Mutual information therefore penalizes transformations that decrease the amount of information in the separate images. However, it is still not completely immune to the overlap problem, but less than joint entropy.

Another reasonable interpretation of mutual information is that it measures the amount of information A contains about B and, as $MI(A, B) = MI(B, A)$, the amount of information B contains about A. Hence, it is mutual information. This can be seen from [45]:

$$MI(A, B) := H(B) - H(B|A) \, , \tag{4.10}$$

where $H(B|A)$ is the conditional entropy based on the conditional density $p_{B|A}(b|a)$, the chance of the intensity value b in the image B given that the corresponding intensity in the image A has the value a. The maximization of mutual information such that the amount of information the images contain about each other is maximal should find the deformation that registers the two images.

A last well-known definition of mutual information makes use of the so-called Kullback-Leibler divergence, which is a measure of the distance between two densities [45]:

$$MI(A, B) := \int_{-\infty}^{\infty} \int_{-\infty}^{\infty} p_{A,B}(a, b) \log \frac{p_{A,B}(a, b)}{p_A(a) p_B(b)} da db \, . \tag{4.11}$$

It therefore measures the distance between the joint density of the images' intensities and the density $p_A p_B$, which is equal the joint density if the two densities are independent. In this case mutual information reaches its minimum. According to this, mutual information is a measure of dependence between the two images. The assumption is that there is maximal dependence between the intensities when the images are correctly aligned.

It is important to note that all three definitions of mutual information given by equations (4.9), (4.10) and (4.11) are identical and can be rewritten into each other [45].

Since mutual information is based on the joint density of the images' intensities instead of the intensity values directly and as it reduces the overlap problem compared to joint entropy, it is commonly used for automatic intermodality registration. Therefore, the distance measure for the non-parametric registration problem stated by equation (4.3) and used for the pseudo CT generation is suggested to be defined as:

$$D[R, T_{\boldsymbol{u}}] := MI(R, T_{\boldsymbol{u}}) \, . \tag{4.12}$$

Curvature Registration The recommended regularization to control the deformation of the non-parametric registration used by the presented approach for CT prediction is based on second order derivatives:

$$S[\boldsymbol{u}] := \frac{1}{2} \sum_{l=1}^{3} \int_{\boldsymbol{\Omega}} (\Delta u_l(\boldsymbol{x}))^2 d\boldsymbol{x} \, , \tag{4.13}$$

This regularizing term was introduced by Fischer and Modersitzki [37, ch. 12] in order to circumvent the pre-registration required by other registration techniques such as elastic, fluid and diffusion registration. However, according to Modersitzki, the main point is not that the additional pre-registration becomes redundant but that the registration becomes less dependent on the initial position of the reference and template images. Nevertheless, the initial position still plays an important role and it is not advisable to skip the pre-registration. The integrand of S given by equation (4.13) might be viewed as an approximation of the curvature. Thus, the idea of the regularizer is to minimize the curvature of the components of the deformation. Therefore, this type of registration is called curvature registration. A property of curvature registration is that the transformation will be smoother than the ones obtained by a registration based on first order derivatives regularizers, like diffusion.

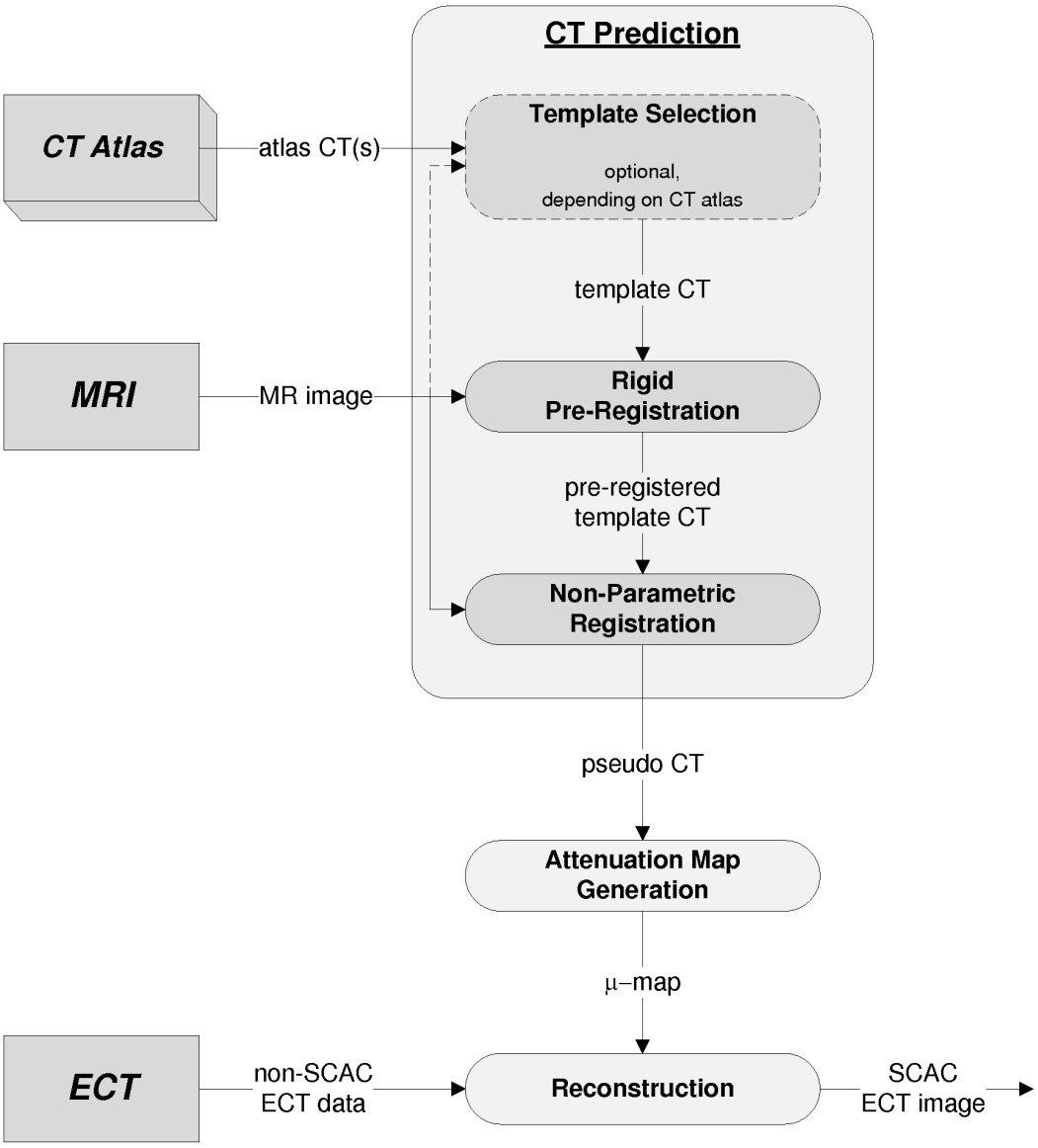

Figure 4.2: Compact flow chart expanded on the CT prediction

4.3 Attenuation Map Generation

After the pseudo CT is obtained, which is considered to be an approximation of an actual CT scan of the studied patient, well known CT-based techniques can be applied to determine the patient-specific attenuation map. At the energies of X-ray spectra, photoelectric interactions contribute significantly to the attenuation of photons especially for bone but less for soft tissue. Moreover, these interactions with matter are almost negligable in ECT especially in PET. Hence, simple uniform scaling of the CT numbers is not sufficient and lacks accuracy at most for bone. Therefore, commercial hybrid ECT-CT systems established in clinical environments commonly make use of the bilinear scaling method described in section 3.2.2 to translate the CT numbers of the sequentially acquired CT image to attenuation coefficients, since it considers the difference in scaling for bone and soft tissue. Consequently, the bilinear scaling is also the method of choice to generate an attenuation map from the predicted CT. The compact flow chart expanded on the generation of the attenuation map is shown in Figure 4.3.

The suggested bilinear function to translate the CT numbers H to the corresponding linear attenuation coefficients μ in particular reads as follows:

$$\mu = \begin{cases} \mu_{\text{water}} \, \frac{H+1000}{1000}, & H \leq 0 \\ \mu_{\text{water}} + H \, \frac{\mu^{\text{CT}}_{\text{water}}(\mu_{\text{bone}} - \mu_{\text{water}})}{1000(\mu^{\text{CT}}_{\text{bone}} - \mu^{\text{CT}}_{\text{water}})}, & H > 0 \end{cases}, \tag{4.14}$$

where μ^{CT}_{water} and $\mu^{\text{CT}}_{\text{bone}}$ are the estimated attenuation coefficients of water and bone at the effective CT energy and μ_{water} and μ_{bone} are, analogously, the theoretic attenuation coefficients of water and bone at the emission photon's energy.

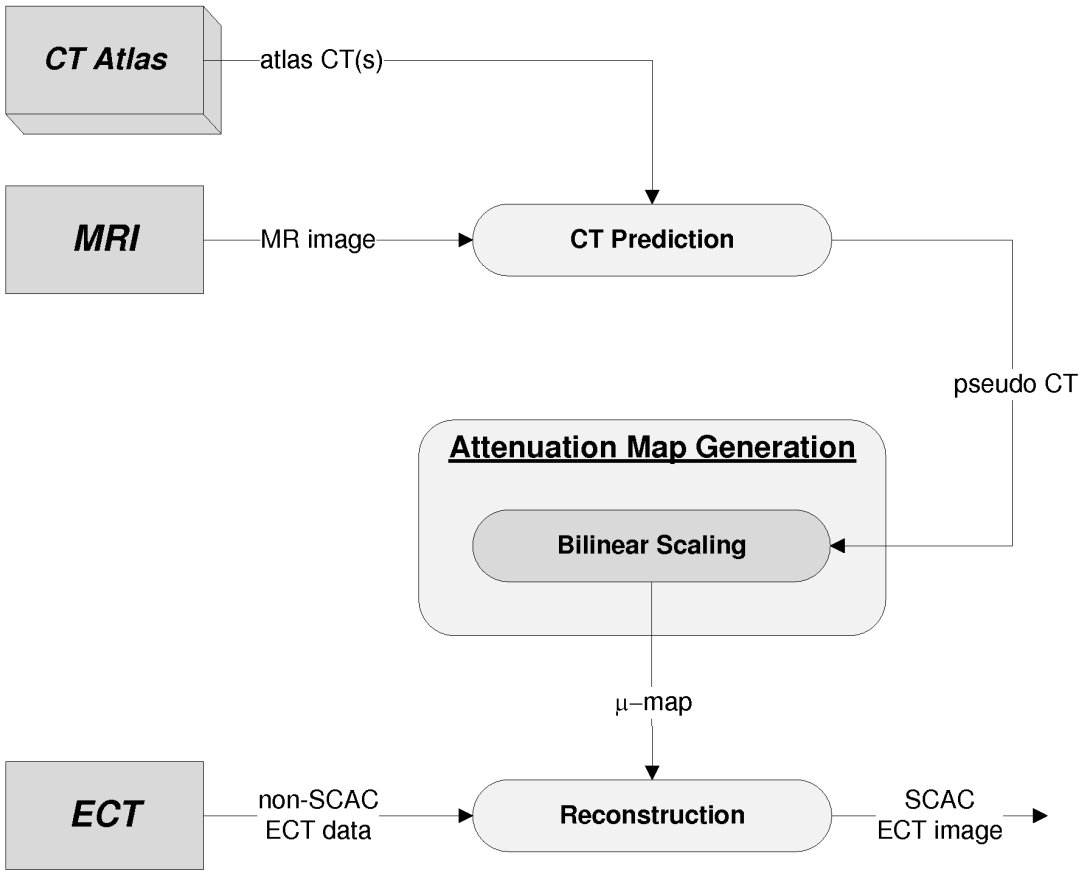

Figure 4.3: Compact flow chart expanded on the attenuation map generation

4.4 Reconstruction

The correction of the emission data for photon attenuation is carried out during the reconstruction process. As noted in section 2.4, the attenuated radon transform in SPECT given by equation (2.9) cannot be inverted analytically. Therefore, iterative reconstruction algorithms are commonly applied in SPECT. These algorithms incorporate the knowledge of the attenuation coefficients given by the obtained attenuation map into the successive forward and backward projections. Besides, a scatter model based on the attenuation of the different tissues can be incorporated the same way. When applying attenuation correction, also correcting for scatter is recommended. Otherwise, overcorrection may occur, cf. section 2.3.2. The emission data in PET, however, can be corrected for attenuation before the actual reconstruction as shown already in section 2.4. The sinogram of the ACFs, cf. equation (2.11), is computed by forward projecting the attenuation coefficients. Then the uncorrected PET sinogram is multiplied with the sinogram of the ACFs to get the attenuation corrected PET sinogram, cf. equation (2.12). Before, a scatter correction method that also makes use of the attenuation map is commonly applied. However, as both scatter and attenuation correction in PET are just multiplicative corrections of the measured emission data, the order is not of importance. After that, the corrected PET data is reconstructed using FBP reconstruction algorithms. Nevertheless, iterative reconstruction algorithms are nowadays commonly applied in PET as well.

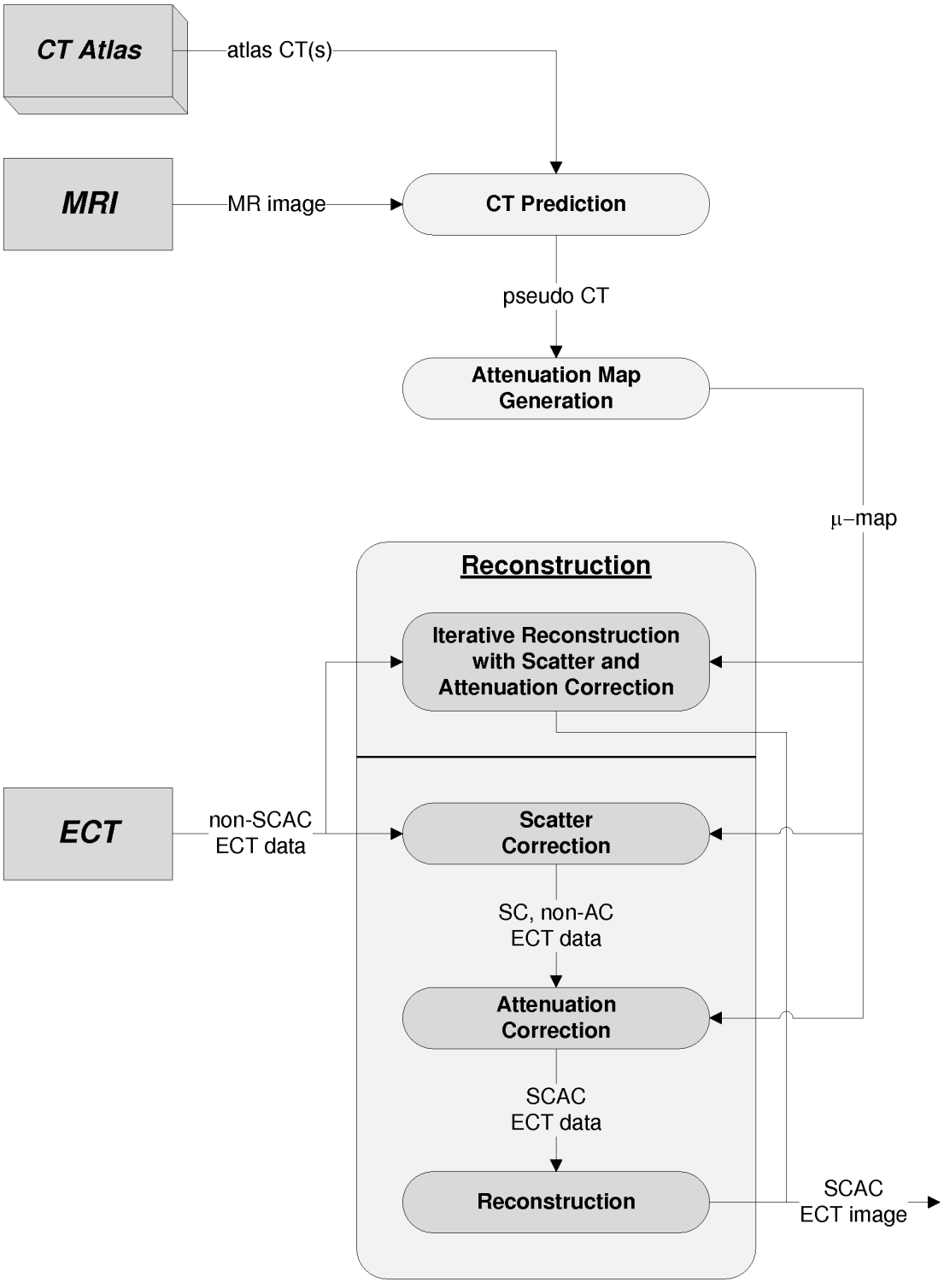

Figure 4.4: Compact flow chart expanded on the reconstruction

Chapter 5

Evaluation

In the previous chapter an approach to compensate emission data for photon attenuation that makes use of a co-registered MR image and an atlas CT to generate a pseudo CT of the patient which then is translated to an attenuation map was introduced and described in detail. The evaluation of the feasibility of this approach was the goal of this study. As the generation of an attenuation map from a co-registered CT image, as considered in section 3.2.2, is currently prior art for combined SPECT-CT and PET-CT scanners, this step does not pose a problem. Therefore, the pseudo CT prediction is the linchpin of the entire approach. Hence, evaluating the robustness and accuracy of the CT prediction based on non-parametric registration is fundamental for demonstrating the feasibility of the approach. Moreover, the accuracy of such generated pseudo CT has to be shown, where the pseudo CT has to be as accurate as necessary to get corrected emission images which are clinical acceptable. On the other hand, the CT prediction strongly depends on the CT atlas and the used template selection strategy. However, the evaluation of these issues is left open because the sound expedience of the pseudo CT generation based on non-parametric registration only has to be shown first.

The materials and methods applied for evaluation are summarized in this chapter. Afterwards, the results of the evaluation are presented and discussed visually.

5.1 Materials and Methods

As there was no PET-MR scanner available for the evaluation, clinical data acquired at the Universitätsklinikum Erlangen on a PET-CT scanner (Biograph 64, Siemens Medical Solutions, Erlangen) and a stand-alone MR scanner (Magnetom Trio-Tim, Siemens Medical Solutions, Erlangen) was adopted. The co-registered CT of the PET-CT image pair was considered as gold standard for the CT prediction, since it is an actual X-ray transmission scan of the patient also used for attenuation correction by the reconstruction algorithm of the PET-CT scanner. In addition, because the MR image was not aligned with the PET data, the CT image of the PET-CT image pair was used to determine the rigid transformation that registers the MR image with the PET data, simulating a simultaneous PET-MRI acquisition. A rigid transformation was sufficient, as only brain studies were evaluated. Figure 5.2 illustrates the flow chart of the CT prediction adapted for evaluation.

The CT atlas used for evaluation consisted of three head CTs. Two of them were extracted from CT images of whole-body scans. The whole-body CTs were acquired at the Universitätsklinikum Erlangen on the PET-CT scanner, whereas the other head CT was captured on a stand-alone CT scanner (Somatom Sensation 64, Siemens Medical Solutions, Erlangen). Consequently, the two atlas CTs extracted from the whole-body CTs showed less resolution than the third one, whereas this pictured the upper half of the head only. Some acquisition and reconstruction characteristics of the atlas CTs are summarized in Table 5.1. Moreover, Figure 5.1 draws example slices of the atlas CT images, in particular, one slice per transversal, sagittal and coronal plane of each.

The registration algorithms applied for evaluation were implemented by Hahn and Daum, both PhD students at the Chair of Pattern Recognition and furthermore the main academic advisors of the work at hand. The implementation of these algorithms is based on the numerical schemes derived by Modersitzki [37], where the mathematical problem of non-parametric registration was defined as in equation (4.3) with mutual information as distance measure, cf. equation (4.12), and regularized by curvature, cf. equation (4.13). Moreover, the non-parametric registration employed a multi-level approach. Therefore, a registration pyramid with a given number of levels L is created, where the registration on level $l \in [1..L]$ is carried out with the images downsampled by a factor of $1/2^{L-l}$. The initial transformation on the first level is the identity and on the higher levels the transformation resulting from the registration on the preceding level.

The clinical software InSpace 2008 was used for the evaluation. It is a volume imaging application for interactive viewing of volume data that is exclusively developed for Siemens Medical Solutions by HipGraphics Inc., Baltimore, and mainly be used in the research of medical image processing algorithms. An important aspect of this volume imaging application is that it maintains a plugin interface. This enabled the integration of specially designed plugins developed for the evaluation of the pseudo CT generation based on non-parametric registration. The rigid registration tool supplied by Hahn and Daum was also integrated in InSpace.

The main plugin of the evaluation toolkit encapsulated the non-parametric registration and provided an interface for other plugins to adjust its parameters and to enforce the consecutive execution of defined workflow steps. These steps are the import of the reference and template from InSpace, the pre-processing, the actual non-parametric registration, the post-processing of the registration results and finally the upload of the post-processed registered template. Besides, all results, including intermediate ones such as the pre-processed volumes, can be retained by other plugins for further processing or output. The user transformation of the pre-registration and a by manual cropping defined region of interest are optionally considered during the import. The pre-processing includes the resampling of the imported images such that the resampled images cover the same physical extent and are sampled on the same discrete grid, matching the resolution of both images. The parameters of the non-parametric registration are the number of levels used for the multi-level registration, the stopping criteria at the last level which get automatically relaxed for the other levels, the stiffness of the deformation and the distance measure to use. The stiffness represents the parameter α in equation (4.4) which determines the amount of regularization, where the stiffness is not α directly. The higher the stiffness, the more regularization of the deformation takes place and vice versa. When mutual information is used as distance measure, the Parzen estimation of the joint density is influenced by the number of histogram bins and the kernel width specified relative to the width of a single histogram bin. Finally, the optional post-processing resamples the registered template, either to the original size of the imported template or to a specific size or resolution.

A second plugin provided the user interface to the main plugin to guide through the steps of the workflow and to enable the setting of the parameters for different evaluation studies. Screenshots of the user interface are shown in Figure 5.3 for each particular workflow step.

To assist the analysis of the evaluation, two further plugins recorded the parameter settings during the execution and sampled intermediate results such as the pre-processed template and the joint histogram used to measure the mutual information. Thereby, a third plugin encapsulated the output operations and a last plugin provided a user interface to store loaded or uploaded volumes.

label	Atlas 1	Atlas 2	Atlas 3
body part	head	head	head (upper half)
sex	female	female	unknown
size	192 x 235	219 x 300	512 x 512
number of slices	117	120	28
pixel spacing (mm x mm)	0.95 x 0.95	0.95 x 0.95	0.65 x 0.65
slice thickness (mm)	2.00	2.00	4.00
scanner	Biograph 64	Biograph 64	Somatom Sensation 64
low dose	yes	yes	no

Table 5.1: Overview of atlas CTs used for evaluation

The post-processing and analysis of the generated pseudo CTs was accomplished by taking advantage of the capabilities of a prototyping environment. This Image Processing and Prototyping Environment (IPE) was developed by the author of the work at hand while working as a student assistant at the Chair of Pattern Recognition. It enables the creation of image processing networks consisting of data processing modules, which can have inputs, produce outputs and are controlled by adjustable parameters. The main application of the IPE is the IPE Network Editor, a graphical user interface for creating, editing, configuring and executing such networks. Having an IPE network defined and stored as network description file, another application, called IPE Network Runner, can be used to execute the network from the command line with specified parameters passed as command arguments. Moreover, a plugin for InSpace 2008 exists, that integrates the IPE into InSpace.

Applying the introduced materials and methods, the evaluation studies basically complied with the following protocol. First, the co-registered MR image of the patient whose PET data is to be corrected and a CT image manually selected from the CT atlas are loaded in InSpace. Optionally, the atlas CT image is manually cropped such that the template CT used for the CT prediction covers only the body part pictured by MRI. Next, the template CT is automatically pre-registered with the MR image using the rigid registration plugin, with manual adjustment if needed. Then, the plugin for logging the parameters and the plugin for sampling intermediate and final results are configured and attached to the main plugin. The reference and template are now imported and pre-processed by the main plugin as described before, whereby the images are downsampled to reduce the complexity of the non-parametric registration. Then, the non-parametric registration is performed and the registered template is optionally upsampled afterwards. To visually assess the resulting pseudo CT it is uploaded in InSpace.

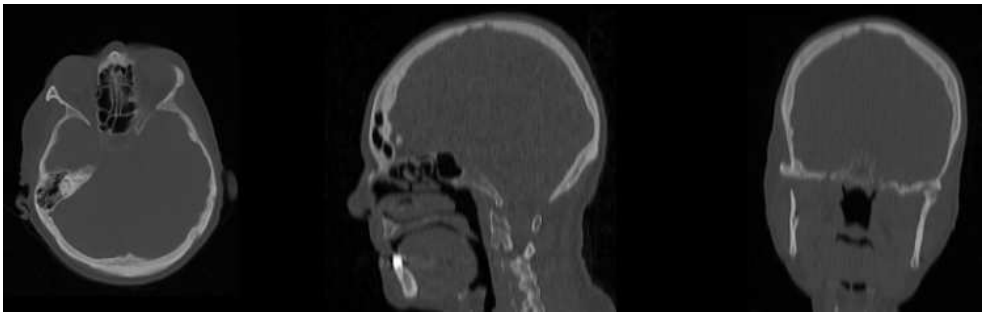

(a) Atlas 1

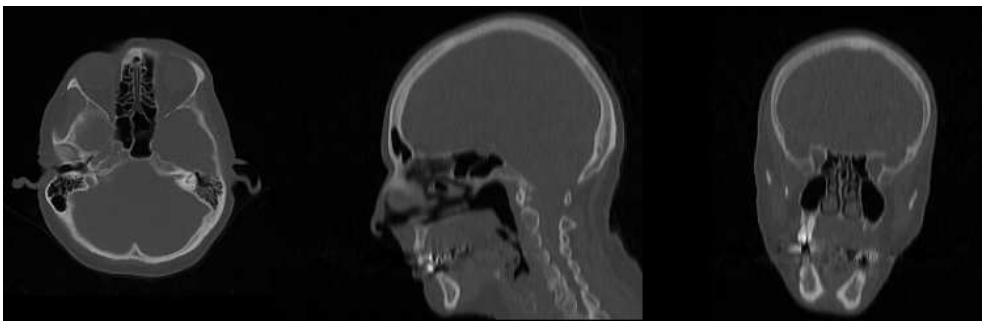

(b) Atlas 2

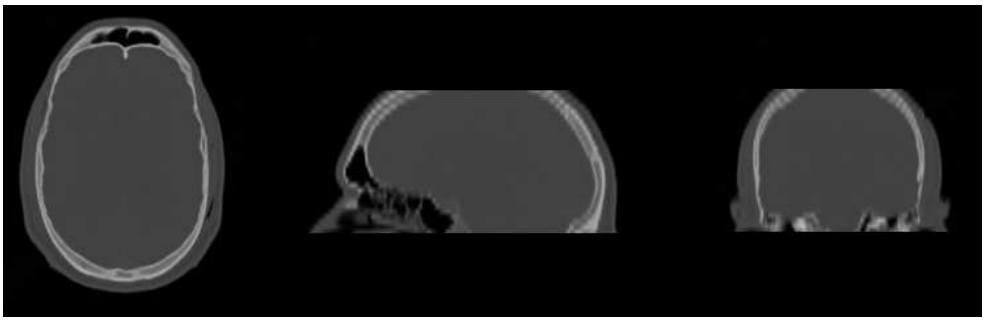

(c) Atlas 3

Figure 5.1: Example slices of the atlas CTs used for evaluation

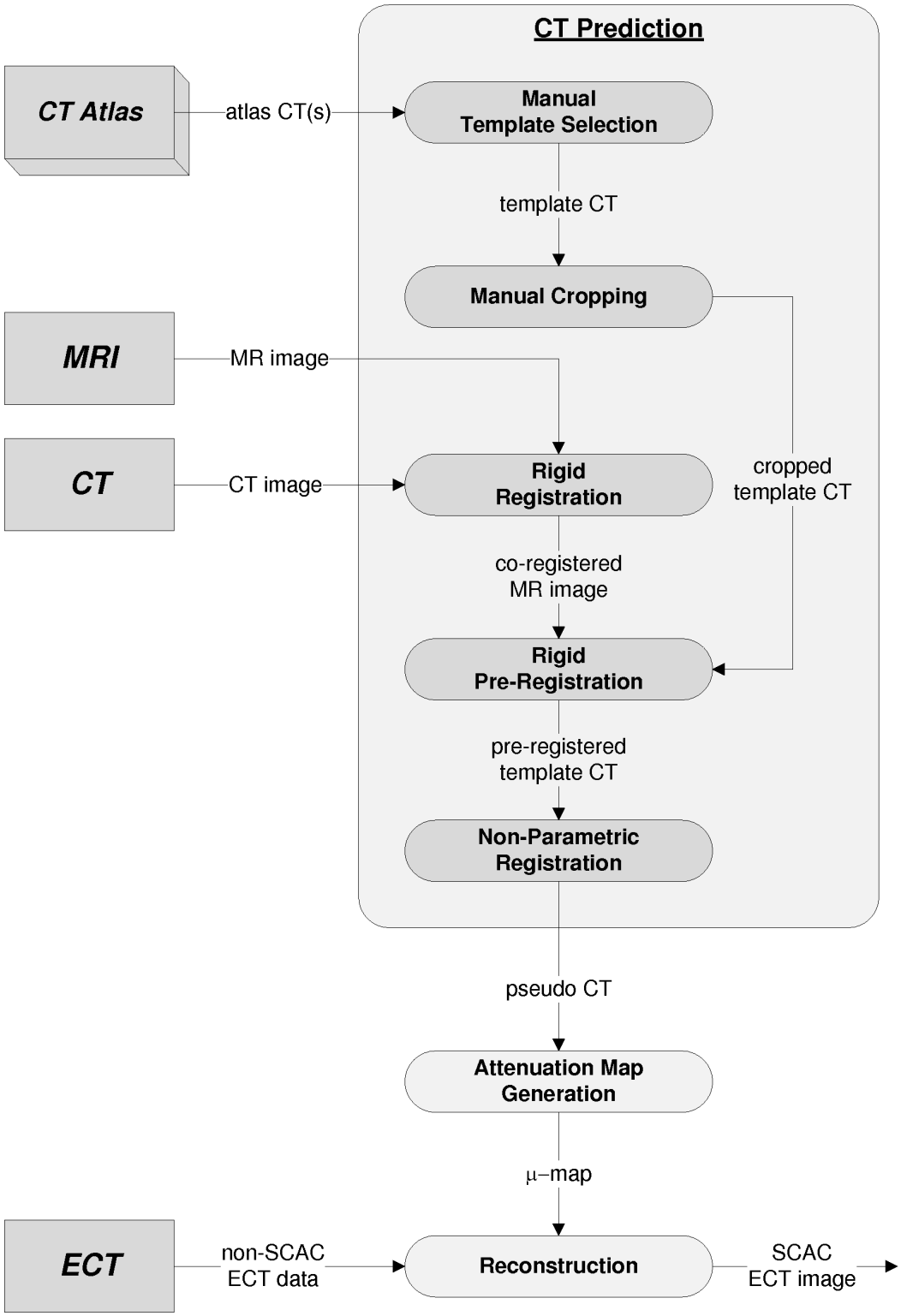

Figure 5.2: Compact flow chart expanded on the CT prediction adapted for evaluation

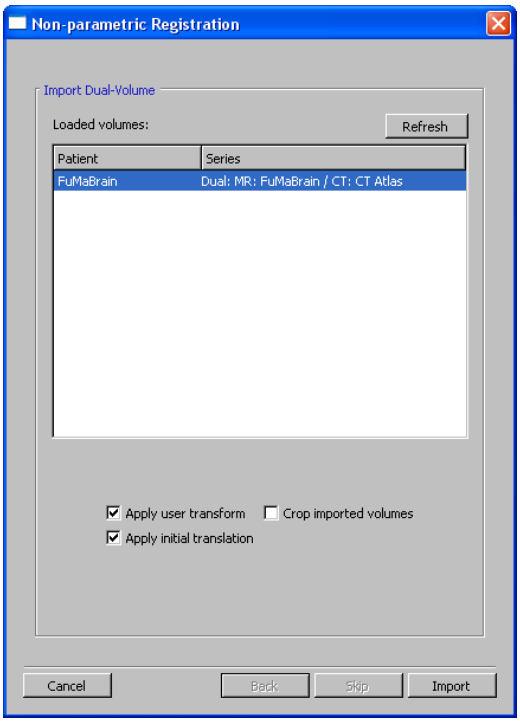

(a) Import pre-registered images

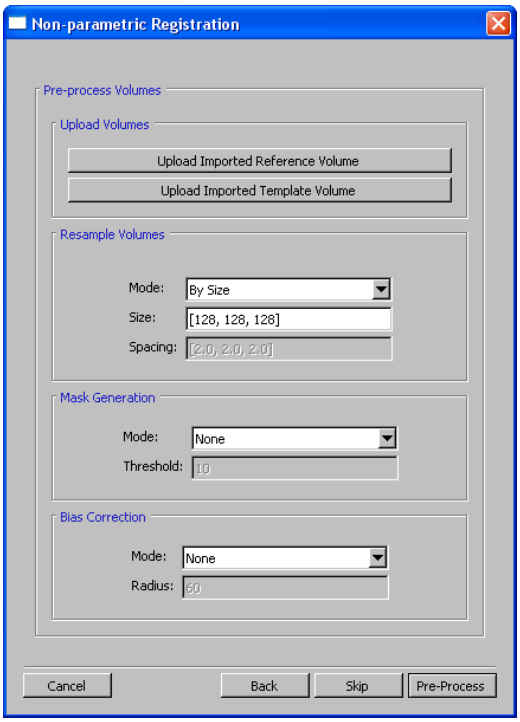

(b) Pre-process imported images

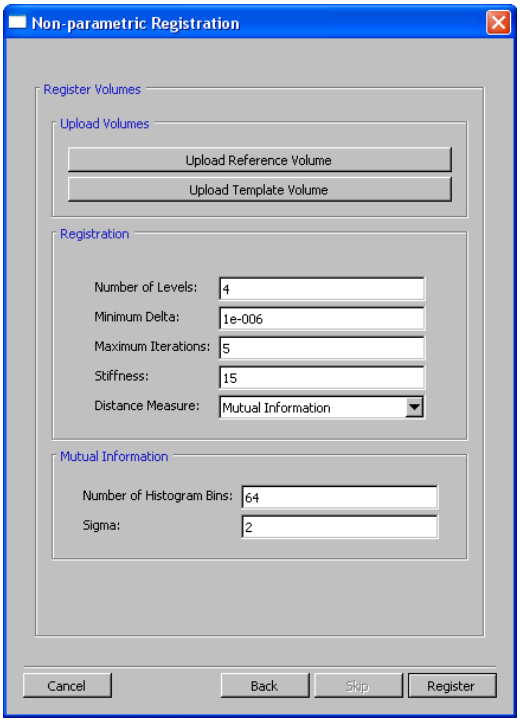

(c) Register pre-processed images

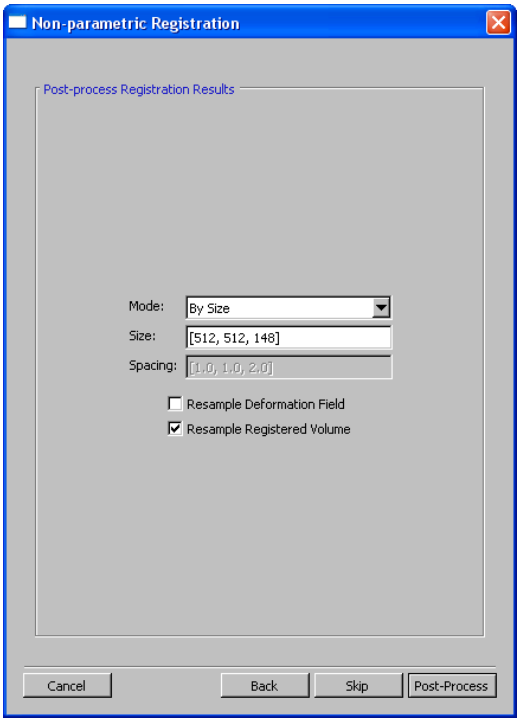

(d) Post-process registered template

Figure 5.3: Step-by-step user interface to the non-parametric registration

5.2 Results

As there was only appropriate data of PET-CT and MRI acquisitions of a single subject available, the evaluation was based on just one brain imaging study. Therefore, the quantitative measurements have minor statistical meaning. They are computed to assess the results of the investigated study not only visually and, nonetheless, underline the proof of concept. Clearly, the evaluation can demonstrate initial results only but no conclusive statement about the reliability or robustness of the evaluated method can be made. However, the feasibility of the method can be delineated to some degree. Example slices of the brain CT, MR and PET images of the patient used for evaluation are drawn in Figure 5.4.

Pseudo CTs were generated using each of the three atlas CTs one at a time as template. Common parameter settings for the pseudo CT generation are outlined in what follows, s.a. Table 5.2. The reference MR and template CT were downsampled to an image size of 128 x 128 x 128, matching the resolution to 1.96 x 1.96 x 1.74 mm^3. Moreover, the non-parameteric registration was performed on four levels with a maximum of 20, 15, 10 and 5 iterations at each according level. Another stopping critera was a minimum absolute value of the distance measure, termed minimum delta, of 10^{-6}. The number of histogram bins used to determine the histogram of discrete intensity values was equal 64 and the width of the Gaussian kernel functions used for the density estimation was set to two times of the width of a single histogram bin. Afterwards, the generated pseudo CTs were upsampled again to match the size and resolution of the actual CT of the patient.

The parameter that influences the registration result at most is the amount of regularization, the value of the stiffness parameter, accordingly. Therefore, this parameter was adjusted in a first evaluation study with one common atlas CT as template and the different resulting pseudo CTs were compared both to the gold standard and to each other for determining the range of appropriate values for the stiffness of reasonable deformations. For that reason, mean absolute value differences were computed and assessed both visually and quantitatively. For the computation of the difference image between a specific pseudo CT and the actual CT, the images were resampled on a common grid with a uniform spacing of 1 x 1 x 1 mm^3, resulting in a size of 249 x 249 x 222. Furthermore, the background of both was normalized in the following sense. All intensities of the pseudo CT that had a value below a threshold of -750 HU were set to -1024 HU, the intensity value corresponding to air. Then, all intensities in the actual CT, where the corresponding intensities in the pseudo CT showed that background value were also set to -1024 HU. This way, both images comprised the same foreground region with removed background noise, while especially the borders of the pseudo CT were not defined after deformation.

Another reason for this was that the actual CT pictured also the scanner table while the atlas CTs did not. By applying the mentioned steps, this table was removed from the actual CT, too. Otherwise, it would have caused high differences, misleading the computation of the mean value. Figure 5.5 plots the set values of the stiffness parameter to the corresponding mean normalized difference value. However, the mean absolute difference values without this normalization are given for comparison reasons as well in Figure 5.7. Moreover, as bone contributes considerably more to attenuation especially in PET, Figure 5.6 plots the mean difference value that was computed by ignoring the intensities below 0 HU. From these plots, it can be concluded that the stiffness parameter value should be chosen within the range of 20 to 30.

After the range of appropriate stiffness parameter values has been investigated, the stiffness parameter for generating pseudo CTs using all three atlas CTs as template was set to 22.5, as this value obtained the best mean normalized difference value for the atlas CT Atlas 1. Example slices of the resulted pseudo CTs are shown by Figure 5.8. Moreover, Figure 5.9 illustrates the normalized difference relative to the actual CT of the patient, where the images are drawn inverted to improve the contrast. Additionally, the mean differences of these pseudo CTs are summarized in Table 5.3. Thus, the mean of the mean normalized difference values is 40.9 HU, which is decisively better than the average absolute error value of 100.7 HU reported by Hofmann et al. [21] on their pseudo CT prediction method. Even if this value is compared to the non-normalized difference values, except the one of the pseudo CT generated from the atlas CT that comprises the upper half of the head only, it shows that the mean of the mean difference values of the other two pseudo CTs is lower than the one reported by the authors. However, it has to be emphasized that only three pseudo CTs were generated, where one has been used to determine the optimal stiffness parameter. Moreover, these pseudo CTs were generated for a single patient compared to the 17 patients envolved by the evaluation of Hofmann et al.

pre-processing	
size	128 x 128 x 128
pixel spacing (mm x mm)	1.96 x 1.96
slice thickness (mm)	1.74
non-parametric registration	
number of levels	4
maximum iterations	5
minimum delta	10^{-6}
number of histogram bins	64
kernel width (relative to histogram bin width)	2.0
post-processing	
size	512 x 512 x 148
pixel spacing (mm x mm)	0.94 x 0.94
slice thickness (mm)	1.5

Table 5.2: Common settings of pseudo CT generation

atlas CT	Atlas 1	Atlas 2	Atlas 3
mean normalized difference (HU)	45.41	46.98	30.26
mean water/bone mixtures difference (HU)	29.73	28.80	30.26
mean difference (HU)	89.66	90.10	166.43

Table 5.3: Mean differences of pseudo CTs generated from the three different atlas CTs, with the stiffness parameter set to 22.5

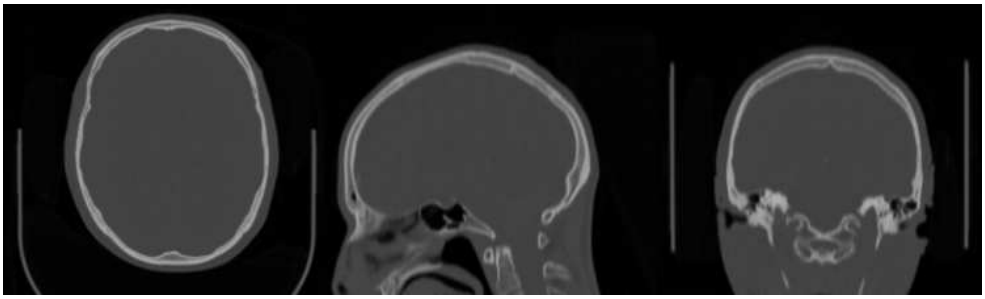

(a) CT image

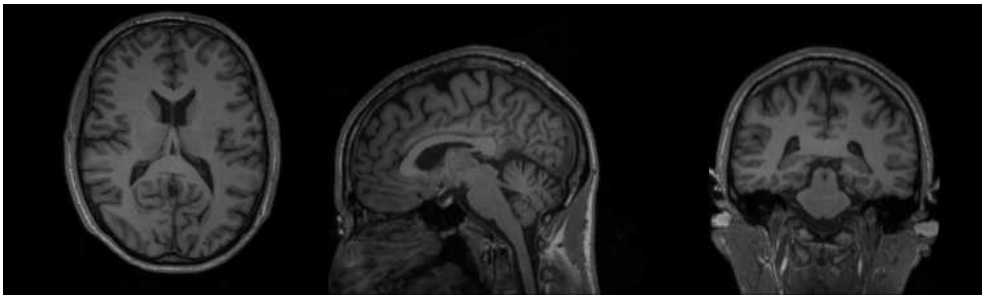

(b) MR image

(c) non-AC PET image

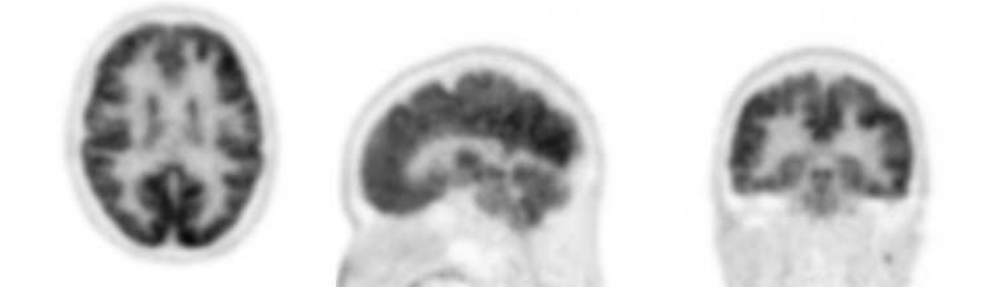

(d) AC PET image

Figure 5.4: Example slices of the brain images of the patient used for evaluation, where the MR image was rigidly registered with the CT image

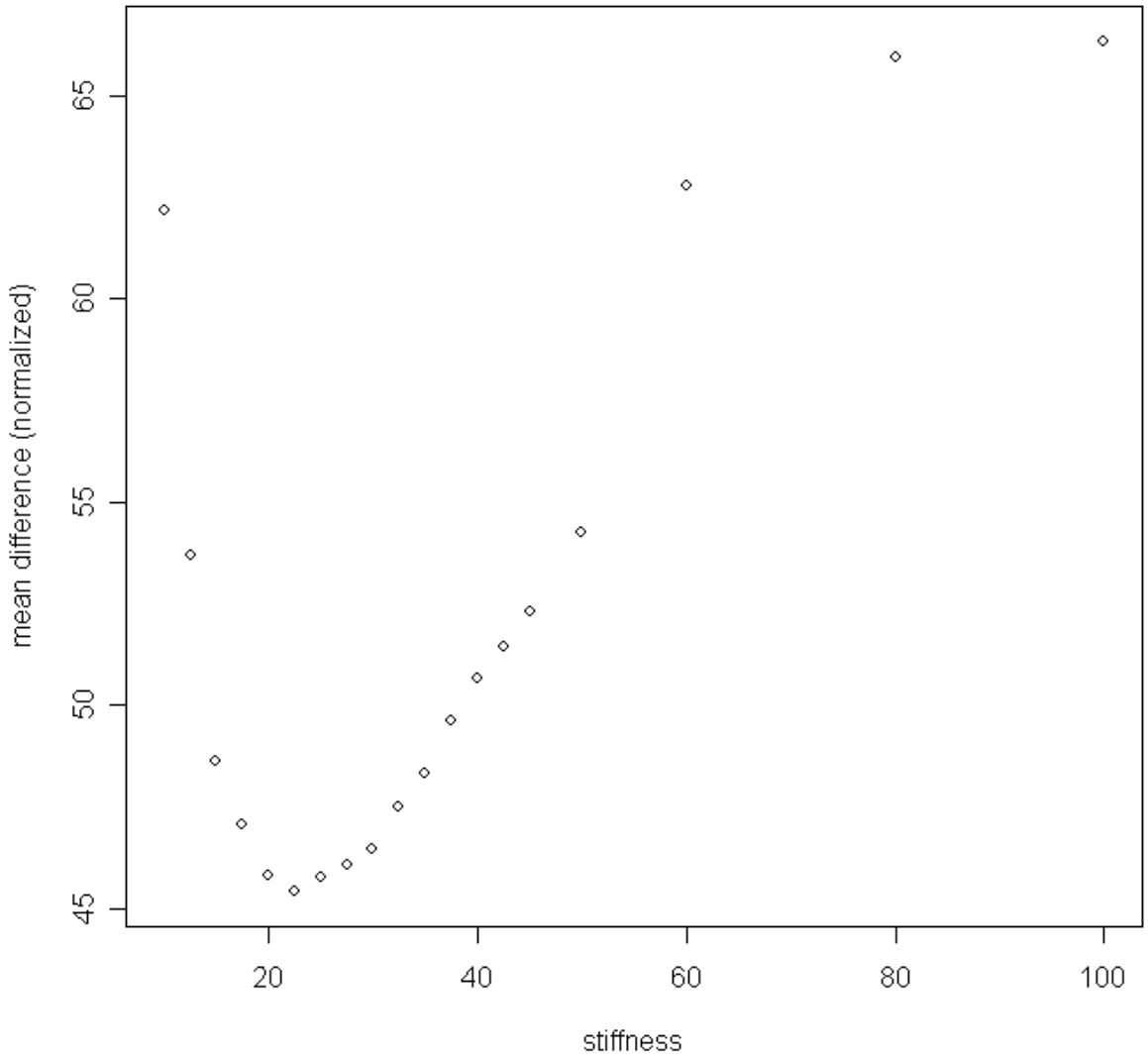

Figure 5.5: Mean normalized difference values resulting from the pseudo CTs generated with varying stiffness from the atlas CT Atlas 1 as template

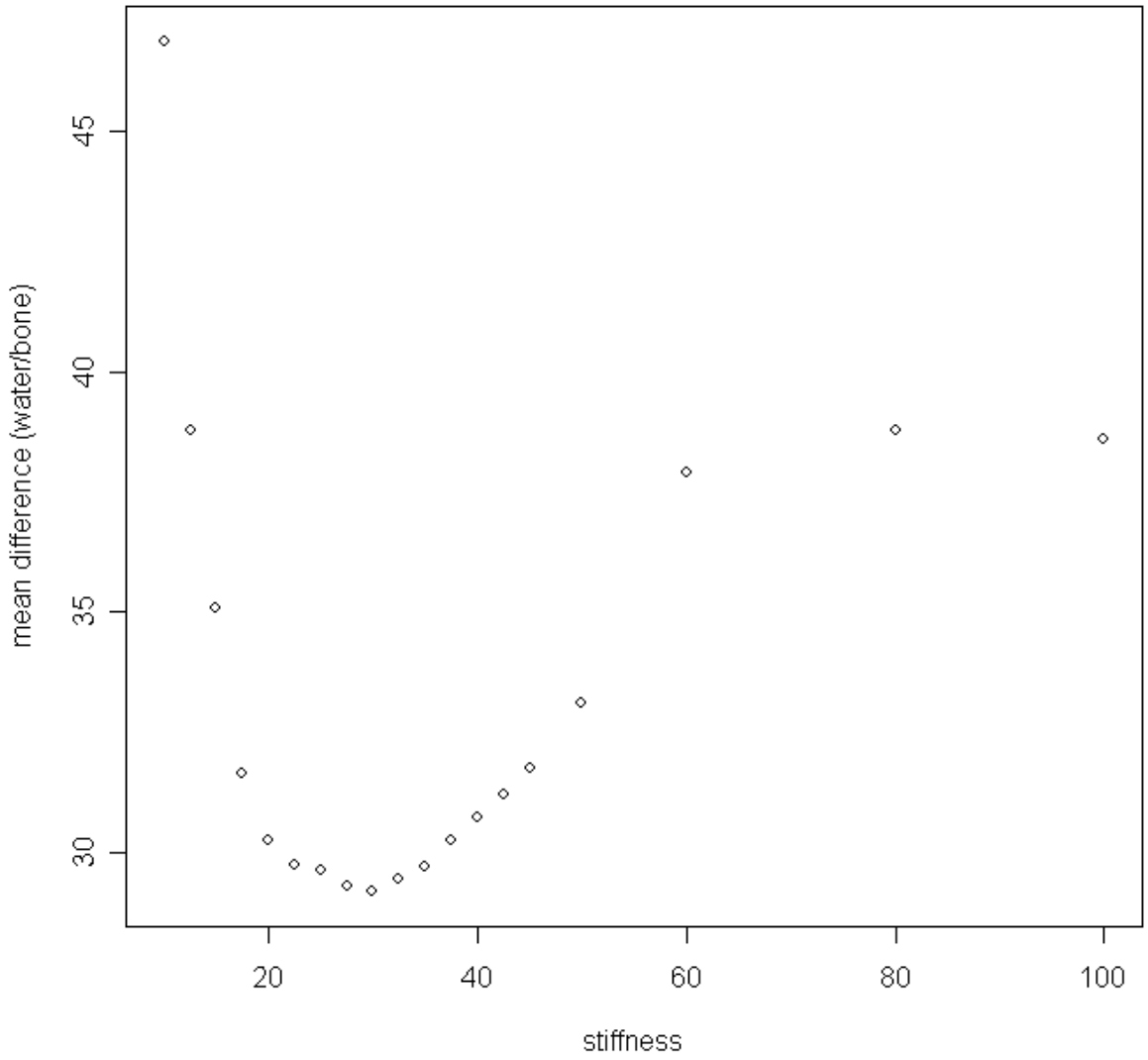

Figure 5.6: Mean water/bone mixtures difference values resulting from the pseudo CTs generated with varying stiffness from the atlas CT Atlas 1 as template

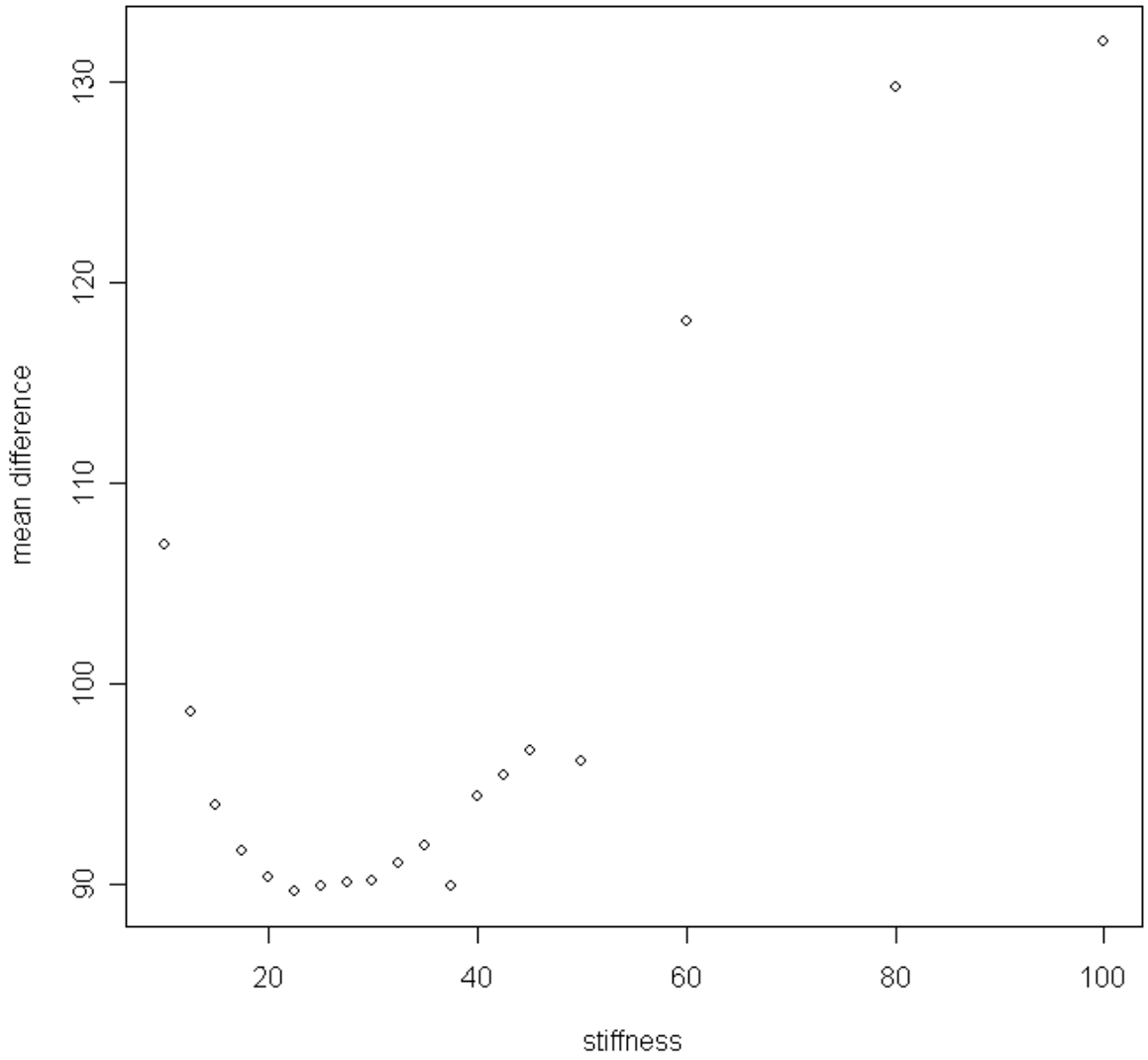

Figure 5.7: Mean difference values resulting from the pseudo CTs generated with varying stiffness from the atlas CT Atlas 1 as template

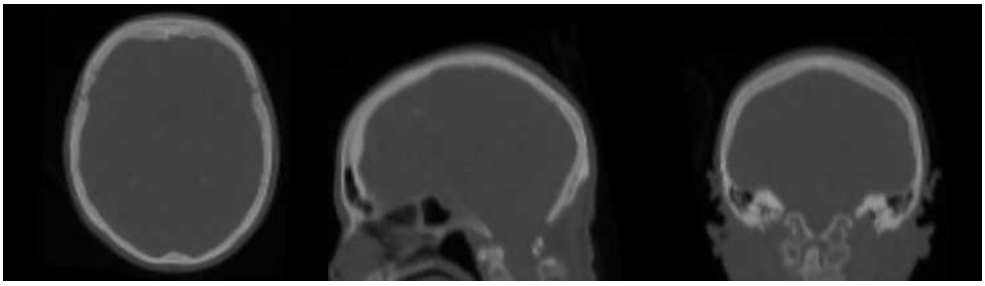

(a) Pseudo CT generated from atlas CT Atlas 1

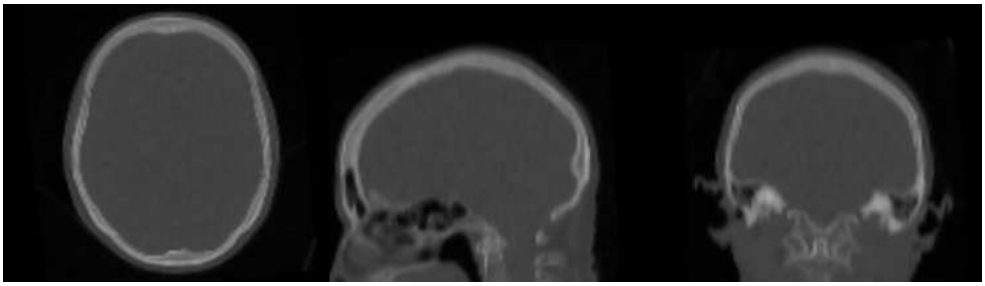

(b) Pseudo CT generated from atlas CT Atlas 2

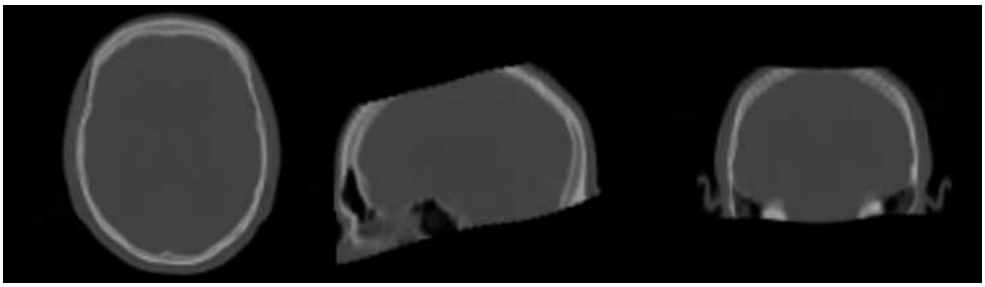

(c) Pseudo CT generated from atlas CT Atlas 3

Figure 5.8: Example slices of the pseudo CTs generated from the different atlas CTs with the stiffness parameter set to 22.5

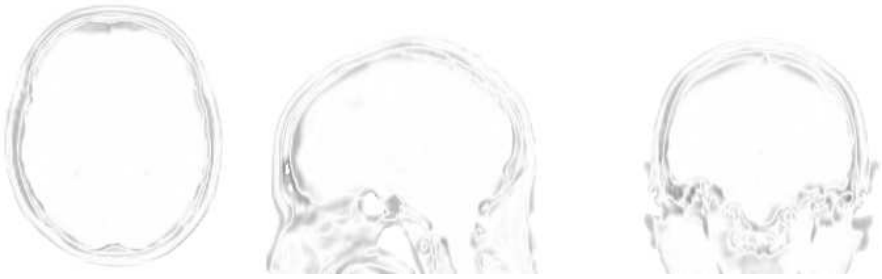

(a) Difference image of the pseudo CT generated from atlas CT Atlas 1

(b) Difference image of the pseudo CT generated from atlas CT Atlas 2

(c) Difference image of the pseudo CT generated from atlas CT Atlas 3

Figure 5.9: Corresponding normalized difference images of the pseudo CTs in Figure 5.8 relative to the actual CT of the patient

Chapter 6

Outlook

The employed approach for MRI-guided attenuation correction requires a reliable and locally precise deformable intermodality intersubject registration. More precisely, the deformable registration adapted for the evaluated method is a non-parametric one that does pose the least of all assumptions on the transformation, thus, it provides the most flexibility for the atlas registration. On the other hand, this makes it being quiet prone to finding transformations that yield a pseudo CT which is unlikely a reliable prediction of a transmission scan of the patient's anatomy especially in regions such as the trunk.

The transformation is only restricted by the regularizer, where the amount of regularization is spatially constant. However, as the anatomy varies more in some regions than in others, a locally differing regularization of the transformation should yield more reliable transformations, while introducing this type of prior knowledge. Moreover, as the pseudo CT strongly depends on the atlas CT used as template, a template selection strategy which determines an atlas CT that sufficiently corresponds with the patient is essential.

Otherwise, Hofmann et al. [20] showed on the Joint Molecular Imaging Conference 2007 the reliability of a CT prediction for brain studies based on deformable B-Splines registration, where local inaccuracies of the registration were alleviated combining several atlas registrations, also getting rid of the need for template selection while using the anatomical information of all atlas CTs. Therefore, the combination of the various registered atlas CTs was not just done by averaging, but a more sophisticated regression technique that introduces pattern recognition to attenuation correction. An article on their method, also further investigated in order to augment its applicability to whole-body studies, was most recently submitted by Hofmann et al. [21], where the combination of atlas registration with local pattern recognition is illustrated in more detail.

The results of the various atlas registrations are incorporated as prior knowledge in the following prediction on the basis of pattern recognition methods. According to Hofmann et al., pattern recognition methods for predicting a pseudo CT are motivated by the idea that, while the MR intensity at one spatial location does not contain sufficient information to uniquely determine its tissue class, its neighborhood, however, may add some characteristic information. This may be particularly useful when distinguishing between bone and air as the MR intensity in both cases is near zero. Pattern recognition methods therefore aim at determining a mapping between the intensities of a rectangular patch of the MR image centred at the spatial location of interest and real-valued CT intensities. A training database is created from the matching co-registered atlas MR-CT image pairs and the mapping is obtained by solving a regression problem, where Gaussian Process regression as described in [21] was used by the authors. Finally, the obtained mapping is just applied to the MR image of the patient to get the pseudo CT out of it.

Thus, opposed to the pre-selection of a specific template CT, the pseudo CT generation based on non-parametric registration could, according to the method proposed by Hofmann et al., be carried out for each atlas CT individually followed by regression to tickle the best local fit out of each individual registration. To be able to learn the regression function, however, initial values and target values have to be known for the training database. Therefore, the CT atlas has to be replaced by an atlas consisting of matching MR and CT images, coming up with almost the method proposed by Hofmann et al. with the B-Splines registration substituted by a non-parametric one.

Chapter 7

Summary

The concept of predictive health promotes the goal to detect and treat disease even before it has ever been expressed. Therefore, different imaging modalities visualize different aspects of a disease in a non-invasive way.

Molecular imaging modalities applied in nuclear medicine use tracers of metabolic processes to uncover their spatial distribution within the body. Therefore, the subject has been injected with, has ingested or has inhaled a labeled tracer that radiates photons. Detectors collect the endogeneous photons from outside the body, whereby the measured radiation is directly related to the imaged physiology. The kind of imaged physiology depends on the applied radiopharmaceutical. Tomographic imaging modalities such as SPECT and PET enable the reconstruction of the spatial distribution of radioactivity.

Besides the functional information gained by ECT, anatomical information is often needed to clarify the nature of an abnormality and to help diagnose or stage the underlying disease. Hence, dual-modality imaging is nowadays the prior art in nuclear medicine, where in particular SPECT or PET is combined with CT. This enables a reliable localization of radiopharmaceutical uptake or guides surgery in areas where vital structures neighbor disease or in anatomically complex regions. A major drawback of the combination of ECT and CT is the sequential rather than simultaneous acquisition which frequently introduces misregistrations due to improper patient positioning, respiratory motion and other voluntary patient movement. Moreover, CT gains few soft-tissue contrast and subjects the patient to additional radiation dose.

Contrary, MRI generates high resolution images that yield better soft-tissue contrast and especially a large variety of tissue contrasts. Moreover, it does not require any ionizing radiation and therefore can be used without restrictions in situations where radiation exposure is a concern. Thus, the development of hybrid PET-MRI systems is currently in progress. Those systems will

unify PET, MRI, fMRI and MRS, which may have even more potential as current PET-CT systems. Despite the difficulties that still have to be solved, first human brain images captured with a prototype PET-MRI system already demonstrate the feasibility of this promising combination.

The photons emitted by the radiopharmaceutical interact with the different tissues while traveling through the body. The probability that a photon will undergo an interaction while passing through a unit thickness of tissue is called attenuation coefficient. It is not only dependent on the tissue type but also on the photon's energy. At the photon energies encountered in ECT, the major interactions are photoelectric absorption and Compton scattering, whereas especially in PET Compton scattering dominates considerably. Both absorption and scattering are the components of the general process of photon attenuation. The fundamental relationship of scatter to attenuation can be summarized as follows. An absorption contributes only to attenuation, but scatter increases attenuation and also sets up a potential scatter corruption. Attenuation and scatter have opposite effects on activity quantification in the sense that photon attenuation decreases counts, thus allowing too few photons to be detected, resulting in underestimation of activity. In contrast, scatter corruption increases counts, thus allowing too many photons to be detected, resulting in overestimation of activity. Both attenuation and scatter cause serious artifacts in the reconstructed images, making it difficult or even impossible to read the images properly and to make a reliable diagnose. Particularly, if quantitative analysis of the physiologic process is desired, compensation for photon scatter and attenuation is mandatory.

To enable the compensation for scatter and attenuation, the spatial distribution of attenuation coefficients has to be known. This knowledge can then be either incorporated into an iterative reconstruction algorithm or the emission data can be corrected exactly before the actual reconstruction in PET as the attenuation of photons in PET is independent of the point of emission. Thus, attenuation correction strategies try to determine the attenuation map which represents the spatial distribution of attenuation coefficients. The prior art of these methods are calculated, transmission-based, atlas-based or MRI-guided methods.

Calculated approaches try to determine the body contour from the emission data alone and then assign a uniform distribution of attenuation coefficients to the inside of the body. As the resulting attenuation map is uniform, these methods are only appropriate for brain studies but more adequate methods must be performed where the attenuation coefficient distribution is not known a priori and also for regions of inhomogeneous attenuation. To account for the considerable higher attenuation of the skull, a larger coefficient can be assigned within a certain thickness of the outline or by estimating the skull boundary from an uncorrected reconstruction.

The most accurate attenuation correction methods are the measured methods that apply an additional transmission scan of the patient.

In radionuclide transmission imaging an external single-photon or positron emitting source is placed on one side of the patient and a detector on the other side measures the transmitted photons before, during or after emission scanning. The attenuation map can then be reconstructed from the natural logarithm of the blank-to-transmitted sinogram ratios, where the blank scan is performed while no patient is present in the FOV. To reduce the total acquisition time in sequential transmission imaging, short transmission scans are usually done, increasing noise in transmission images and therefore introducing noise in the corrected emission images. Several approaches such as the segmentation of the reconstructed attenuation map and non-linear filtering have been proposed to reduce the noise. Using single-photon emitting sources also in PET made simultaneous transmission-emission imaging possible which has proven to be very practical especially in whole-body oncology studies. When the photon energy in transmission imaging is not the same as in emission imaging, which is particularly the case in simultaneous transmission-emission imaging, the reconstructed attenuation map has to be properly scaled.

CT-based attenuation correction is the method of choice for hybrid ECT-CT systems. The advantages are the high resolution transmission images with much lower noise, the short transmission times and that it is no longer necessary to include external radionuclide sources. However, as the X-ray source emits photons which cover a relatively broad energy spectrum compared to the mono-energetic photons emitted by the radiopharmaceutical, the translation of measured attenuation coefficients to the emission photons' energy is more difficult. Basically five methods have been proposed: segmentation, uniform scaling, bilinear scaling, hybrid segmentation/scaling and dual-energy decomposition. The bilinear scaling is currently the most widely applied method. It can be considered as combining an air/water mixture model for CT numbers less than zero and a water/bone mixture model otherwise.

Atlas-based methods try to derive the attenuation map from an atlas of attenuation coefficients scaled to the appropriate photon energy. This is accomplished by anatomic standardization using deformable image registration. A conceptual limitation of proposed approaches is that existing patient-specific anomalies cannot be modeled in an atlas obtained from a single or even an average representation of the population.

The goal of MRI-guided attenuation correction is to derive the attenuation map from an MR image of the patient whose emission data is to be corrected. This kind of attenuation correction is very attractive for hybrid PET-MRI systems. However, the main difficulty is to find a mapping between the non-standardized, by means of magnetic field inhomogeneities distorted MR

intensities and the appropriate energy-dependent attenuation coefficients. Because of that, few publications addressed this type of non-uniform attenuation correction so far. Three different approaches have been proposed: a segmentation-based approach, a MRI-guided atlas-based approach and most recently an approach that combines pattern recognition and atlas registration, The method evaluated in this work follows the second.

The evaluated approach for attenuation correction predicts an X-ray transmission scan of the patient based on the anatomical information provided by MRI. Therefore, CT numbers are obtained from a suitable atlas CT using non-parametric image registration with mutual information as distance measure and regularized by curvature. Then, well-known CT-based techniques to determine the attenuation map from the generated pseudo CT can be applied. The common bilinear scaling method is suggested to be used to translate the CT numbers to properly scaled attenuation coefficients. The flow of data and the steps deployed to determine the patient-specific attenuation map from the co-registered MR image are summarized in Figure 7.1.

The evaluation was performed with visual assessment and quantitative analysis. The CT prediction was in the spotlight of this evaluation, since the generation of the attenuation map from a CT image of the patient is yet commonly applied by hybrid PET-CT systems. To maintain the evaluation, a protocol was defined and an evaluation toolkit was implemented. The CT prediction was adapted for evaluation as there was no PET-MR scanner available. Instead, clinical data acquired on a PET-CT and a stand-alone MR scanner were used, where the MR image was rigidly registered with the CT of the PET-CT image pair to align it with the PET data. As only few studies with a PET-CT and an appropriate MR scan of the same patient were available during this work, the evaluation could only be carried out for a single brain study. First, the optimal value for the stiffness parameter of the applied non-parametric registration algorithm was determined by quantitative analysis of the mean differences. These differences were computed for pseudo CTs generated from the same atlas CT but with varying stiffness. For each of these pseudo CTs, a mean normalized difference value was obtained in the sense that the background of both the pseudo CT and the actual CT was matched and intensities below a lower threshold were set to -1024 HU. It turned out that the optimal stiffness parameter lies in the range of 20 to 30. Consequently, a stiffness parameter of 22.5 was used for the following generation of pseudo CTs from the available atlas CTs. The mean of the mean normalized difference values of the pseudo CTs was 40.9 HU.

To improve the results of the non-parametric registration, prior knowledge in the form of locally dependent regularization could be implemented instead of just a global degree of regularization, considering that anatomy varies in some regions more than in others. Moreover, to

predict a CT of the patient more reliable and robust and opposed to the pre-selection of a specific template CT, the pseudo CT generation based on non-parametric registration could be carried out for each atlas CT individually followed by regression to tickle the best local fit out of each individual registration. To be able to learn the regression function, however, initial values and target values have to be known for the training database.

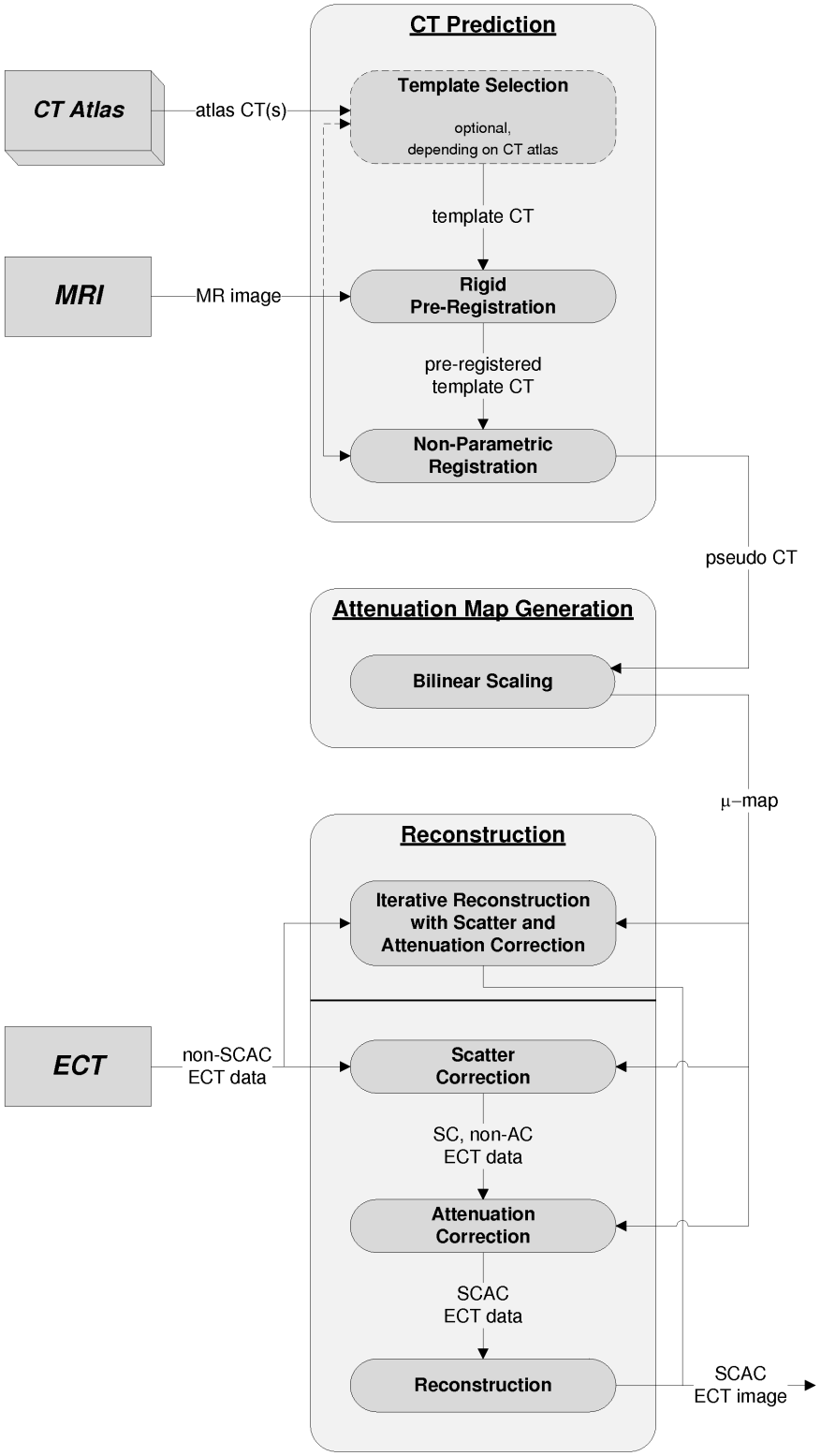

Figure 7.1: Flow chart of the MRI-guided CT prediction method

Appendix A

Related Patents

While methods for scatter and attenuation correction of prior art and most recently developed methods are considered in chapters 3 and 6 and while the MRI-guided CT prediction method evaluated in this work is yet concisely compared to these approaches where reasonable, patents and patent applications of the most similar ones of these methods are delineated in this appendix, where the evaluated method is distinguished from the claimed methods.

The atlas-based IAD method for scatter and attenuation correction introduced in section 3.3.1 was disclosed through the patent application [46] and is protected by the European patent [47] and the United States patent [54]. These patents protect the idea of using a computer model of the density distribution within the region of interest aligned with the emission image to guide scatter and attenuation correction. In general, the claimed method comprises the steps of aligning a 3D computer model representing the density distribution with the emission data and applying scatter and attenuation correction using the aligned computer model as a guide. In particular, the used computer model is in the form of an atlas that consists of two components, a functional and an anatomical one, where the functional component is used for aligning the atlas with a preliminary reconstruction of the emission data and the anatomical component simulates a transmission scan used for scatter and attenuation correction. Although, the approach evaluated in this work as well comprises atlas registration to align a transmission scan with the emission data, the alignment is carried out by registration of the atlas with an already co-registered MR image and not by direct alignment of the atlas with the emission data to be corrected. Thus, even though the presented approach is similar to the patented method, actually, this method is not claimed by these patents.

Krieg et al. have submitted the patent application [31] of their proposed NM-MR atlas method introduced in section 3.4.2, which was approved and their method is now protected by the United States patent [32]. This method adapts an already co-registered MR image of the patient for atlas registration, where the atlas again consists of two components, a reference MRI acquisition and a correction data set, that are connected to each other either directly or indirectly. If connected directly, the reference MR image and the correction data set are stored in a common matrix, thus, a data point of the correction data set is assigned to each data point of the MR image. Otherwise, if the data sets are connected indirectly, intervals of MR intensities of the reference MR image are mapped to specific correction values, where the mapping is determined by classification of the reference MR intensities into most likely tissue types and then assigning known correction values to each tissue class. Adapting this NM-MR atlas for MRI-guided attenuation correction, the reference MR image is registered with the MR image of the patient and the obtained transformation is then applied to the correction data set. Although the evaluated method is quite similar to the method protected by the patent [32] with the correction data set consisting of proper CT numbers, the evaluated method decisively discriminates itself by means of the determination of the transformation that aligns the transmission component of the atlas with the emission data. Whereas this transformation is determined adapting an NM-MR atlas and MR-MR registration in case of the claimed method, it is determined by direct registration of the transmission atlas with the MR image of the patient in case of the evaluated method. Therefore, the reference MR image is no longer needed and a usual transmission atlas remains.

There was also a patent application submitted by Pichler et al. [43] regarding their most recently published MRI-guided method for scatter and attenuation correction introduced in the outlook. Unless this method applies MRI-guided atlas registration and a prediction of a pseudo CT of the patient as well, it predicts the pseudo CT more sophisticated adapting also pattern recognition methods compared to a usual atlas registration as applied in case of the evaluated method. In particular, the perspective is turned on a point of view that centers on finding a mapping between MR intensities and real-valued CT numbers using pattern recognition techniques such as Support Vector Machines to solve the regression problem. Thereby, the atlas registration with the MR image of the patient is adapted to gain some kind of prior knowledge that can be considered while building the training data set for determining such a mapping.

List of Figures

List of Tables

List of Abbreviations

2D	Two Dimensional
3D	Three Dimensional
AC	Attenuation Correction/Attenuation Corrected
ACF	Attenuation Correction Factor
APD	Avalanche Photodiode
CT	Computer Tomography
DETECT	Dual Energy Transmission Estimation Computed Tomography
ECT	Emission Tomography
EM	Expectation Maximization
FBP	Filtered Backprojection
FCM	Fuzzy C-means
fMRI	Functional Magnetic Resonance Imaging
FOV	Field of View
HU	Hounsfield Units
IAD	Inferring-Attenuation Distributions
IPE	Image Processing and Prototyping Environment
LOR	Line of Response
LSO	Lutetium Oxyorthosilicate
MI	Mutual Information
ML-EM	Maximum Likelihood Expectation Maximization
MR	Magnetic Resonance
MRI	Magnetic Resonance Imaging
MRS	Magnetic Resonance Spectroscopy
NM-MR	Nuclear-medical Magnetic Resonance
OS-EM	Ordered Subsets Expectation Maximization
PET	Positron Emission Tomography

PMT	Photomultiplier Tube
SAC	Segmented Attenuation Correction
SC	Scatter Correction/Scatter Corrected
SCAC	Scatter and Attenuation Corrected
SET	Simultaneous Emission and Transmission Measurements
SNR	Signal-to-noise Ratio
SPECT	Single Photon Emission Tomography
SSD	Sum of Squared Differences

Bibliography

[1] S. Alenius, U. Ruotsalainen, and J. Astola. Attenuation correction for PET using count-limited transmission images reconstructed with median root prior. *IEEE Trans. Nucl. Sci.*, 46(3):646–651, June 1999.

[2] H. O. Anger. Scintillation camera. *Rev. Sci. Instrum.*, 29(1):27–33, January 1958.

[3] C. Bai, P. E. Kinahan, D. Brasse, C. Comtat, D. W. Townsend, C. C. Meltzer, V. Villemagne, M. Charron, and M. Defrise. An analytic study of the effects of attenuation on tumor detection in whole-body PET oncology imaging. *J. Nucl. Med.*, 44:1855–1861, 2003.

[4] T. Beyer, P. E. Kinahan, D. W. Townsend, and D. Sashin. The use of X-ray CT for attenuation correction of PET data. *IEEE Nucl. Sci. Symp. Med. Imaging Conf. Rec.*, 4:1573–1577, 30 Oct.-5 Nov. 1994.

[5] S. C. Blankespoor, X. Wu, K. Kalki, J. K. Brown, H. R. Tang, C. E. Cann, and B. H. Hasegawa. Attenuation correction of SPECT using x-ray CT on an emission-transmission CT system: Myocardial perfusion assessment. *IEEE Trans. Nucl. Sci.*, 43(4):2263–2274, August 1996.

[6] C. Burger and G. K. von Schulthess. *Functional Imaging*, chapter 5, pages 157–216. Lippincott-Raven Publishers, Philadelphia, 1998.

[7] C. Burger, G. Goerres, S. Schoenes, A. Buck, A. H. R. Lonn, and G. K. von Schulthess. PET attenuation coefficients from CT images: experimental evaluation of the transformation of CT into PET 511-keV attenuation coefficients. *Eur. J. Nucl. Med.*, 29:922–927, 2002.

[8] C. Catana, Y. W. M. S. Judenhofer, J. Qi, B. J. Pichler, and S. R. Cherry. Simultaneous acquisition of multislice PET and MR images: Initial results with a MR-compatible PET scanner. *J. Nucl. Med.*, 47(12):1968–1976, December 2006.

[9] A. Celler, K. L. Dixon, Z. Chang, S. Blinder, J. Powe, and R. Harrop. Problems created in attenuation-corrected SPECT images by artifacts in attenuation maps: A simulation study. *J. Nucl. Med.*, 46:335–343, 2005.

[10] S. R. Deans. *The Radon transform and some of its applications*. John Wiley & Sons Inc., New York, 1983.

[11] O. Demirkaya. Anisotropic diffusion filtering of PET attenuation data to improve emission images. *Phys. Med. Biol.*, 47:N271–N278, 2002.

[12] R. A. de Kemp and C. Nahmias. Attenuation correction in PET using single photon transmission measurement. *Med. Phys.*, 21(6):771–778, June 1994.

[13] O. Dössel. *Bildgebende Verfahren in der Medizin: von der Technik zur medizinischen Anwendung*, chapter 6, pages 157–184. Springer, Berlin, 2000.

[14] R. O. Duda, P. E. Hart, and D. G. Stork. *Pattern Classification*. John Wiley & Sons Inc., New York, 2nd edition, 2001.

[15] J. M. Fröhlich, A. P. Schubiger, and G. K. von Schulthess. *Functional Imaging*, chapter 2, pages 25–60. Lippincott-Raven Publishers, Philadelphia, 1998.

[16] G. Glatting, M. Wuchenauer, and S. N. Reske. Iterative reconstruction for attenuation correction in positron emission tomography: Maximum likelihood for transmission and blank scan. *Med. Phys.*, 26(9):1838–1842, September 1999.

[17] S. Goetze, T. L. Brown, W. C. Lavely, Z. Zhang, and F. M. Bengel. Attenuation correction in myocardial perfusion SPECT/CT: Effects of misregistration and value of reregistration. *J. Nucl. Med.*, 48(7):1090–1095, July 2007.

[18] M. J. Guy, I. A.Castellano-Smith, M. A. Flower, G. D. Flux, R. J. Ott, and D. Visvikis. DETECT - Dual Energy Transmission Estimation CT - for improved attenuation correction in SPECT and PET. *IEEE Trans. Nucl. Sci.*, 45(3):1261–1267, June 1998.

[19] G. V. Heller, J. Links, T. M. Bateman, J. A. Ziffer, E. Ficaro, M. C. Cohen, and R. C. Hendel. American society of nuclear cardiology and society of nuclear medicine joint

position statement: Attenuation correction of myocardial perfusion spect scintigraphy. *J. Nucl. Cardiol.*, 11:229–230, 2004.

[20] M. Hofmann, F. Steinke, V. Scheel, M. Brady, B. Schölkopf, and B. J. Pichler. MR-based PET attenuation correction: Method and validation. Joint Mol. Imaging Conf. 2007, Providence, RI, USA.

[21] M. Hofmann, F. Steinke, V. Scheel, G. Charpiat, J. Farquhar, P. Aschoff, M. Brady, B. Schölkopf, and B. J. Pichler. MR-based attenuation correction for PET/MR: A novel approach combining pattern recognition and atlas registration. J Nucl Med (in press).

[22] H. M. Hudson and R. S. Larkin. Accelerated image reconstruction using ordered subsets of projection data. *Trans. Med. Imaging*, 13(4):439–446, December 1994.

[23] M. S. Judenhofer, H. F. Wehrl, D. F. Newport, C. Catana, S. B. Siegel, M. Becker, A. Thielscher, M. Kneilling, M. P. Lichy, M. Eichner, K. Klingel, G. Reischl, S. Widmaier, M. Rocken, R. E. Nutt, H.-J. Machulla, K. Uludag, S. R. Cherry, C. D. Claussen, and B. J. Pichler. Simultaneous PET-MRI: a new approach for functional and morphological imaging. *Nat. Med.*, 14(4):459–465, 2008.

[24] A. C. Kak and M. Slaney. *Principles of Computerized Tomographic Imaging*. IEEE Press, 1988.

[25] J. S. Karp, G. Muehllehner, H. Qu, and X.-H. Yan. Singles transmission in volume-imaging PET with a ^{137}Cs source. *Phys. Med. Biol.*, 40:929–944, 1995.

[26] M. A. King, B. M. W. Tsui, and T.-S. Pan. Attenuation compensation for cardiac single-photon emission computed tomographic imaging: Part 1. impact of attenuation and methods of estimating attenuation maps. *J. Nucl. Cardiol.*, 2:513–524, 1995.

[27] P. E. Kinahan, D. W. Townsend, T. Beyer, and D. Sashin. Attenuation correction for a combined 3D PET/CT scanner. *Med. Phys.*, 25(10):2046–2053, October 1998.

[28] P. E. Kinahan, B. H. Hasegawa, and T. Beyer. X-ray-based attenuation correction for positron emission tomography/computed tomography scanners. *Sem. Nucl. Med.*, XXXIII(3):166–179, July 2003.

[29] K. Kitamura, H. Iida, M. Shidahara, S. Miura, and I. Kanno. Noise reduction in PET attenuation correction using non-linear gaussian filters. *IEEE Trans. Nucl. Sci.*, 47(3):994–999, June 2000.

[30] G. Kontaxakis and L. G. Strauss. Maximum likelihood algorithms for image reconstruction in positron emission tomography, 1998.

[31] R. Krieg, R. Ladebeck, and O. Schreck. Method for generating an MR atlas and for MR imaging using same. U. S. Pat. App. No. US 2006/0058641 A1, March 2006.

[32] R. Krieg, R. Ladebeck, and O. Schreck. Method for generating an MR atlas and for MR imaging using same. U. S. Pat. No. US 7,327,138 B2, February 2008.

[33] K. J. LaCroix, B. M. W. Tsui, B. H. Hasegawa, and J. K. Brown. Investigation of the use of X-ray CT images for attenuation compensation in SPECT. *IEEE Trans. Nucl. Sci.*, 41(6):2793–2799, December 1994.

[34] J. E. Mackewn, D. Strul, W. A. Hallett, P. Halsted, R. A. Page, S. F. Keevil, S. C. R. Williams, S. R. Cherry, and P. K. Marsden. Design and development of an MR-compatible PET scanner for imaging small animals. *IEEE Trans. Nucl. Sci.*, 52(5):1376–1380, October 2005.

[35] S. R. Meikle, M. Dahlbom, and S. R. Cherry. Attenuation correction using count-limited transmission data in positron emission tomography. *J. Nucl. Med.*, 34(1):143–150, January 1993.

[36] S. R. Meikle, D. L. Bailey, P. K. Hooper, S. Eberl, B. F. Hutton, W. F. Jones, R. R. Fulton, and M. J. Fulham. Simultaneous emission and transmission measurements for attenuation correction in whole-body PET. *J. Nucl. Med.*, 36:1680–1688, 1995.

[37] J. Modersitzki. *Numerical Methods for Image Registration*. Oxford University Press, Oxford, 2004.

[38] M.-L. Montandon and H. Zaidi. Atlas-guided non-uniform attenuation correction in cerebral 3D PET imaging. *NeuroImage*, 25:278–286, 2005.

[39] M.-L. Montandon and H. Zaidi. Quantitative VOI-based analysis of template-guided attenuation correction in 3D brain PET. *IEEE Nucl. Sci. Symp. Conf. Rec.*, 6:3326–3330, 29 Oct.-1 Nov. 2006.

[40] H. Newiger. *Bildgebende Systeme für die medizinische Diagnostik*, chapter 10.2, pages 491–500. Publicis MCD Verlag, Erlangen, 3rd edition, 1995.

[41] J. M. Ollinger. Maximum-likelihood reconstruction of transmission images in emission computed tomography via the EM algorithm. *IEEE Trans. Med. Imaging*, 13(1):89–101, March 1994.

[42] J. A. Patton and T. G. Turkington. SPECT/CT physical principles and attenuation correction. *J. Nucl. Med. Technol.*, 36:1–10, 2008.

[43] B. Pichler, B. S. M. Hofmann, and F. Steinke. Method for determining a property map for an object in particular for a living being base on at least one first image in particular a nuclear magnetic resonance image. WIPO Pat. App. No. WO 2008/006451 A1, January 2008.

[44] J. P. W. Pluim, J. B. A. Maintz, and M. A. Viergever. Interpolation artefacts in mutual information-based image registration. *Comp. Vis. Image Under.*, 77:211–232, 2000.

[45] J. P. W. Pluim, J. B. A. Maintz, and M. A. Viergever. Mutual information based registration of medical images: a survey. *IEEE Trans.Med. Imaging*, 22(8):986–1004, August 2003.

[46] F. S. Prato, R. Z. Stodilka, B. J. Kemp, and R. L. Nicholson. Application of scatter and attenuation correction to emission tomography images using inferred anatomy from atlas. WIPO Pat. App. No. WO 2000/010034 A1, February 2000.

[47] F. S. Prato, R. Z. Stodilka, B. J. Kemp, and R. L. Nicholson. Application of scatter and attenuation correction to emission tomography images using inferred anatomy from atlas. European Pat. Spec. No. EP 1,105,750 B1, October 2004.

[48] A. J. Rockmore and A. Macovski. A maximum likelihood approach to emission image reconstruction from projections. *IEEE Trans. Nucl. Sci.*, 23:1428–1432, 1976.

[49] G. B. Saha. *Physics and Radiobiology of Nuclear Medicine*. Springer New York, Inc., 2nd edition, 2001.

[50] H.-P. Schlemmer, B. Pichler, K. Wienhard, M. Schmand, C. Nahmias, D. Townsend, W.-D. Heiss, and C. Claussen. Simultaneous MR/PET for brain imaging: First patient scans. *J. Nucl. Med.*, 48(Supplement 2):45P, 2007.

[51] Y. Shao, S. R. Cherry, K. Farahani, K. Meadors, S. Siegel, R. W. Silverman, and P. K. Marsden. Simultaneous PET and MR imaging. *Phys. Med. Biol.*, 42:1965–1970, 1997.

[52] L. A. Shepp and Y. Vardi. Maximum likelihood reconstruction in positron emission tomography. *IEEE Trans. Med. Imaging*, 1:113–122, 1982.

[53] R. Z. Stodilka, B. J. Kemp, F. S. Prato, A. Kertesz, D. Kuhl, and R. L. Nicholson. Scatter and attenuation correction for brain SPECT using attenuation distributions inferred from a head atlas. *J. Nucl. Med.*, 41:1569–1578, 2000.

[54] R. Z. Stodilka, F. S. Prato, B. J. Kemp, and R. L. Nicholson. Application of scatter and attenuation correction to emission tomography images using inferred anatomy from atlas. U. S. Pat. No. US 6,740,883 B1, May 2004.

[55] D. W. Townsend and S. R. Cherry. Combining anatomy and function: the path to true image fusion. *Eur. Radiol.*, 11:1968 – 1974, 2001.

[56] C. C. Watson, A. Schaefer, W. K. Luk, and C. M. Kirsch. Clinical evaluation of single-photon attenuation correction for 3D whole-body PET. *IEEE Trans. Nucl. Sci.*, 46(4):1024–1031, August 1999.

[57] B. T. Weinzapfel and G. D. Hutchins. Automated PET attenuation correction model for functional brain imaging. *J. Nucl. Med.*, 42:483–491, 2001.

[58] E. Z. Xu, N. A. Mullani, K. L. Gould, and W. L. Anderson. A segmented attenuation correction for PET. *J. Nucl. Med.*, 32:161–165, 1991.

[59] M. Xu, P. D. Cutler, and W. K. Luk. Adaptive segmented attenuation correction for whole-body PET imaging. *IEEE Trans. Nucl. Sci.*, NS-43:331–336, 1996.

[60] S. K. Yu and C. Nahmias. Single-photon transmission measurements in positron tomography using ^{137}Cs. *Phys. Med. Biol.*, 40:1255–1266, 1995.

[61] H. Zaidi, M. Diaz-Gomez, A. Boudraa, and D. O. Slosman. Fuzzy clustering-based segmented attenuation correction in whole-body PET imaging. *Phys. Med. Biol.*, 47:1143–1160, 2002.

[62] H. Zaidi and B. H. Hasegawa. Determination of the attenuation map in emission tomography. *J. Nucl. Med.*, 44:291 – 315, 2003.

[63] H. Zaidi, M.-L. Montandon, and D. O. Slosman. Magnetic resonance imaging-guided attenuation and scatter corrections in three-dimensional brain positron emission tomography. *Med. Phys.*, 30(5):937–948, May 2003.

[64] H. Zaidi, M.-L. Montandon, and D. O. Slosman. Attenuation compensation in cerebral 3D PET: effect of the attenuation map on absolute and relative quantitation. *Eur. J. Nucl. Med. Mol. Imaging*, 31:52–63, 2004.

[65] H. Zaidi. Is MR-guided attenuation correction a viable option for dual-modality PET/MR imaging? *Radiology*, 244:639–642, 2007.

[66] H. Zaidi. Is radionuclide transmission scanning obsolete for dual-modality PET/CT systems? *IEEE Trans. Nucl. Med. Mol. Imaging*, 34:815–818, 2007.

[67] H. Zaidi, O. Mawlawi, and C. G. Orton. POINT/COUNTERPOINT. Simultaneous PET/MR will replace PET/CT as the molecular multimodality imaging platform of choice. *Med. Phys.*, 34(5):1525–1528, May 2007.

[68] H. Zaidi and M.-L. Montandon. Scatter compensation techniques in PET. *PET Clin.*, 2:219–234, 2007.

[69] H. Zaidi, M.-L. Montandon, and A. Alavi. Advances in attenuation correction techniques in PET. *PET Clin.*, 2:191–217, 2007.

[70] H. Zaidi, M.-L. Montandon, and S. Meikle. Strategies for attenuation compensation in neurological PET studies. *NeuroImage*, 34:518–541, 2007.